The Composite Infrared Spectrometer (CIRS) on Cassini

D. E. Jennings[1,*], F. M. Flasar[1], V. G. Kunde[2], C. A. Nixon[1], M. E. Segura[1,2], P. N. Romani[1], N. J. P. Gorius[1,3], S. Albright[1,4], J. C. Brasunas[1], R. C. Carlson[3], A. A. Mamoutkine[1,5], E. Guandique[1,5], M. S. Kaelberer[1,5], S. Aslam[1], R. K. Achterberg[1,2], G. L. Bjoraker[1], C. M. Anderson[1], V. Cottini[1,2], J. C. Pearl[1], M. D. Smith[1], B. E. Hesman[1,6], R. D. Barney[1], S. Calcutt[7], T. J. Vellacott[8], L. J. Spilker[9], S. G. Edgington[9], S. M. Brooks[9], P. Ade[10], P. J. Schinder[11], A. Coustenis[12], R. Courtin[12], G. Michel[12], R. Fettig[13], S. Pilorz[14], C. Ferrari[15]

[1]*Goddard Space Flight Center, Greenbelt, MD, 20771, USA*
[2]*University of Maryland, College Park, MD 20742, USA*
[3]*The Catholic University of America, Washington, DC 20064, USA*
[4]*the Hammers Company, Inc., Greenbelt, MD 20770, USA*
[5]*ADNET Systems, Inc., Bethesda, MD 20817, USA*
[6]*Space Telescope Science Institute, Johns Hopkins University, Baltimore, MD 21218*
[7]*Department of Physics, University of Oxford, Parks Road, Oxford, OX1 3PU, UK*
[8]*Experian Ltd, London SW1E 5JL, UK*
[9]*Jet Propulsion Laboratory, Pasadena, CA 91109, USA*
[10]*School of Physics and Astronomy, Cardiff University, Cardiff, CF24 3YB, UK*
[11]*Center for Astrophysics and Planetary Science, Cornell University, Ithaca, NY, USA*
[12]*Laboratoire d'Etudes Spatiales et d'Instrumentation en Astrophysique (LESIA), Observatoire de Paris, CNRS, UPMC Univ. Paris 06, Univ. Paris-Diderot, 5, place Jules Janssen, 92195 Meudon Cedex, France*
[13]*Independent Researcher, Eichfeldstr. 3A, 76479 Steinmauern, Germany*
[14]*SETI Institute, Mountain View, CA 94043, USA*
[15]*CEA/Service d'Astrophysique, 91191 Gif-sur-Yvette Cedex, France*
**Corresponding Author: donald.e.jennings@nasa.gov*

Received 11 April 2017; revised XX May, 2017; accepted XX Month XXXX; posted XX Month XXXX (Doc. ID XXXXX); published XX Month XXXX

The Cassini spacecraft orbiting Saturn carries the Composite Infrared Spectrometer (CIRS) designed to study thermal emission from Saturn, its rings and moons. CIRS, a Fourier transform spectrometer, is an indispensable part of the payload providing unique measurements and important synergies with the other instruments. It takes full advantage of Cassini's 13-year-long mission and surpasses the capabilities of previous spectrometers on Voyager *1* and *2*. The instrument, consisting of two interferometers sharing a telescope and a scan mechanism, covers over a factor of 100 in wavelength in the mid- and far-infrared. It is used to study temperature, composition, structure and dynamics of the atmospheres of Jupiter, Saturn and Titan, the rings of Saturn and surfaces of the icy moons. CIRS has returned a large volume of scientific results, the culmination of over thirty years of instrument development, operation, data calibration and analysis. As Cassini and CIRS reach the end of their mission in 2017 we expect that archived spectra will be used by scientists for many years to come.

OCIS codes: *(120.3180) Interferometry; (120.6085) Space instrumentation; (120.6200) Spectrometers and spectroscopic instrumentation; (300.6300) Spectroscopy, Fourier transforms.*

http://dx.doi.org/10.1364/AO.99.0999

1. INTRODUCTION

The Cassini* spacecraft has been orbiting Saturn since July 2004, returning a rich variety of scientific data on the planet, its largest moon Titan, its rings and other moons. An important component of this science has come from the thermal infrared portion of the spectrum, a region covered by the Composite Infrared Spectrometer (CIRS). Thermal infrared spectra contain information about composition, temperature, dynamics and structure of atmospheres and surfaces. CIRS, built by Goddard Space Flight Center [1-3] is the most advanced of a series of infrared Fourier transform spectrometers (FTSs) flown on NIMBUS 3 and 4, Mariner 9 and Voyager 1 and 2 [4-7]. Those previous instruments were all named IRIS (Infrared Interferometer Spectrometer). Voyager IRIS had a single 4.4 milliradian field of view and covered the 200 to 2000 cm^{-1} spectral range with 4.3 cm^{-1} resolution. CIRS was designed to improve on IRIS by sampling many fields of view simultaneously, by extending spectral coverage to longer wavelengths, and by enhancing both spatial and spectral resolutions. The goal was also to increase sensitivity and to provide a selection of spectral resolutions for optimizing the sensitivity for each science goal.

The Cassini-Huygens mission concept was conceived in the early 1980s as an orbiter follow-on to the Voyager reconnaissance flybys of Saturn in 1980 and 1981. A primary purpose of the mission was to perform a comprehensive examination of the complex moon Titan. Although a far-infrared thermal emission spectrometer was listed in the initial versions of the Cassini strawman payload, development of CIRS as a combined mid- and far-infrared instrument did not start until 1987. The instrument and investigation was proposed to NASA in 1990 and selected later that year. The instrument was designed, built, tested and delivered to the Cassini project in the period 1991-96. Cassini was launched on October 15, 1997, encountered Jupiter in December 2000 and went into orbit around Saturn on July 1, 2004. The prime mission ended in 2008, but the general health and success of all spacecraft systems justified extending the mission until 2017. During its thirteen-year tour, almost half a Saturn year, CIRS has studied seasonal changes on Saturn and Titan, warm plume-rich regions of Enceladus' surface, temperature structure of the rings, and surfaces of the smaller moons. Close-up emphasis has been on Titan during 127 targeted flybys. In April 2017 Cassini entered the final phase of its mission, consisting of a series of close "proximal" orbits inside the rings. Cassini will end its life on September 15, 2017 when it undergoes a planned entry into Saturn's atmosphere. By that time CIRS will have collected over 160 million spectra.

During the development of CIRS both an engineering unit and a flight unit were built. Extensive testing of the engineering unit proved to be invaluable and led to design changes in the flight unit and a better understanding of performance prior to flight. The instrument underwent a major design simplification in 1992 during its early development phase as part of an overall descope of the mission and spacecraft. The instrument's original four focal planes were reduced to three (afterwards labeled FP1, FP3 and FP4) and from 21 detector signal channels to 11. Some science capability was inevitably lost, but the descope was beneficial to CIRS in that the optical, mechanical and electronics designs were greatly reduced in complexity, making it possible to build the instrument within constraints on cost and mass.

Development of CIRS was an international collaboration among several institutions. The University of Oxford, UK, provided the 80 K cooler as well as integration and testing of the mid-infrared focal planes. CEA Saclay, France, supplied the photovoltaic detector array. Queen Mary & Westfield College, London, UK, contributed the far-infrared beamsplitter, input polarizer, output polarizer and solar blocker. The University of Karlsruhe, Germany, developed the far-infrared detectors. Observatoire de Paris at Meudon built and tested a prototype of the scan mechanism.

*The Cassini mission is a cooperative project of NASA, ESA (the European Space Agency) and the Italian Space Agency. The Jet Propulsion Laboratory, a division of the California Institute of Technology in Pasadena, CA, manages the mission for NASA's Science Mission Directorate, Washington.

2. INSTRUMENT OVERVIEW

The scientific goals of CIRS on the Cassini mission were to study: 1) the composition, thermal structure and dynamics of the atmospheres of Saturn and Titan; 2) the thermal characteristics and composition of Saturn's rings; and 3) the composition and temperatures of the icy surfaces of the moons. Observations would be global, covering latitude, longitude and altitude, and it was expected that time variability would be found as Saturn and Titan progress through their seasons. The aim was not only to follow up on discoveries made by Voyager, but also to search for new phenomena.

The science requirements of CIRS were driven largely by the improvements over Voyager IRIS that Cassini was expected to achieve at Saturn and Titan (Jupiter science was not a driver of the mission and was not added until after launch). The temperatures of Saturn and Titan place the peaks of their blackbody radiance spectra near 100 cm^{-1}. Thus, much of the spectrum was below the 200 cm^{-1} limit of IRIS. IRIS has a CsI beamsplitter, which at the time it was built had the longest wavelength cut-off among conventional substrate beamsplitters. It was therefore likely that a different technology would be required to reach below 200 cm^{-1}. Planned atmospheric studies included examination of the vertical structure both in composition and temperature. CIRS would need mid-infrared detectors matched to the scale height in Titan's atmosphere, about 40 km. From a flyby distance of 100,000 km this corresponds to a detector field of view of 0.4 mrad, about ten times smaller than the field of view of Voyager IRIS. With the same 50-cm diameter telescope as IRIS, the much smaller detectors of CIRS would demand a greater detector sensitivity, especially since the spectral resolution was required to be improved. This meant that thermopile detectors such as were used in IRIS would not be sufficient for CIRS in the mid-infrared. The search for minor atmospheric constituents drove the requirement on spectral resolution to about an order of magnitude better than IRIS's 4.3 cm^{-1}.

CIRS is a Fourier transform spectrometer, or scanning interferometer [1, 2]. The instrument configured for flight is shown in Fig. 1 and its location on the Cassini spacecraft is indicated in Fig. 2. Instrument parameters for CIRS are listed

in Table 1. CIRS is comprised of two interferometers fed by a common telescope and sharing a scan mechanism (Fig. 3). In the focal plane of the telescope the field image is split between the far-infrared and mid-infrared interferometers. In the far-infrared a Martin-Puplett type polarization interferometer [8, 9] covers the 10 to 600 cm^{-1} portion of the spectrum. In the mid-infrared a conventional Michelson interferometer [10] covers the spectrum in two spectral segments, 580 to 1100 cm^{-1} and 1050 to 1500 cm^{-1}. These two types of interferometer work on different principles. In a polarization interferometer the beamsplitter splits the beam into two orthogonal polarization components. The phase between the two components is varied during the scan so that the polarization state of the recombined beam is modulated. In a conventional Michelson interferometer the beamsplitter splits the amplitude of the electric field into two approximately equal parts. When the phase between the two parts is scanned the interference between the two electric fields in the recombined beam modulates the output intensity. Examples of interferograms recorded in the three spectral segments of CIRS are shown in Fig. 4. The instrument is maintained at 170 K, except for the mid-infrared focal plane, which is kept at around 80 K. Warm electronics (18-22 °C) control the operation and handle the data. A block diagram showing the basic functional components of CIRS is presented in Fig. 5.

The CIRS fields-of-view are shown in Fig. 6. In the far-infrared the scene is viewed with a single field of view 3.9 mrad in diameter [11]. In the mid-infrared the two spectral segments both view the scene with a linear array of ten pixels. Each pixel is 0.27 mrad square full width at half maximum (FWHM) and the separation between detectors is 0.29 mrad. The spectral resolution of CIRS is selected by choosing the scan length. The most commonly used apodized resolutions have been 0.5, 1.0, 3 and 15 cm^{-1}. Three of these resolutions are presented in Fig. 7. We define resolution as FWHM of the instrument lineshape function. An apodized resolution of 0.5 cm^{-1} requires the largest optical path difference to be 2 cm. CIRS records interferograms that are up to 97% one-sided with 3% of the scan before zero-path difference. The total travel of the scan mechanism during a 0.5 cm^{-1} interferogram is 1.1 cm and takes 50 seconds. Selecting shorter scans when less resolution is required allows the user to optimize the use of observing time.

3. OPTICS AND DETECTORS

The optical design of CIRS has been described by Maymon *et al.* [12]. The mechanical and optical layouts of the instrument are shown in Fig. 8. Foreoptics, including a telescope, a field-dividing mirror and a solar blocker, feed the light to the far- and mid-infrared interferometers, and a laser reference interferometer controls the scanning and data sampling in the interferometers.

A. Telescope.

The small detector fields of view and high sensitivity required of CIRS called for a relatively large telescope. Imaging in the mid-infrared demanded that, in the 7-17 μm spectral range, a point source at infinity would be imaged into a spot not more than 0.3 mrad FWHM diameter. The original plan was to use a flight back-up telescope left over from the MIRIS (modified-IRIS) development for Voyager IRIS [13]. However, testing showed that the MIRIS telescope primary mirror, although it met the 4.3 mrad MIRIS imaging requirement, lost its figure upon cooling to 170 K and would not meet the more stringent 0.3 mrad CIRS imaging requirement [14]. In the end, the only hardware from the MIRIS protoflight unit that flew as part of CIRS was the telescope cover, sunshade and secondary baffle (described below).

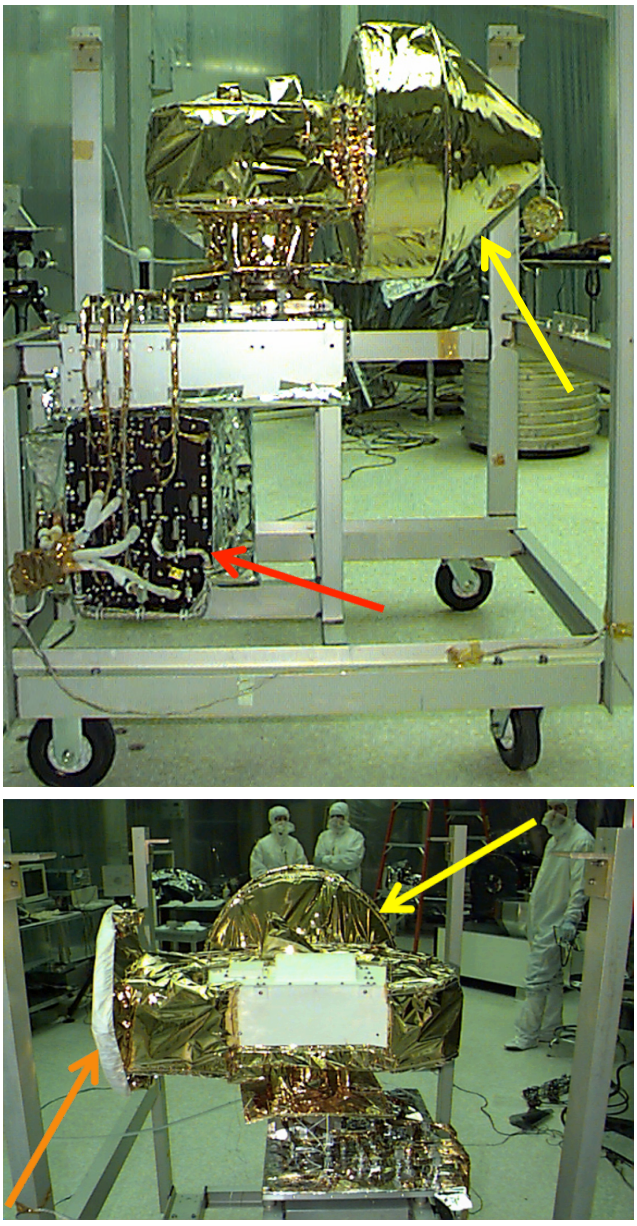

Fig. 1. Views of CIRS from the side (upper panel) and back (lower panel). In these photos covers are installed on the telescope (yellow arrows) and cooler (orange arrow). The CIRS electronics assembly (red arrow) is located below the optics assembly. These photos were taken prior to thermal-vacuum testing.

Fig. 2. Cassini spacecraft with the location of CIRS indicated (arrow). CIRS is mounted on the Remote Sensing Pallet (RSP) furthest from the high gain antenna. (NASA photo.)

A modified primary mirror design was needed, one that was more robust against thermal distortion but which would fit within the same mass and size envelope as the MIRIS primary. The new telescope primary [15], shown in Fig. 9, is a 50.8 cm diameter paraboloid weighing 2.0 kg. Made from beryllium, it has a light-weight stiffening structure on its backside. The primary focuses at f/0.7 onto a 7.6 cm diameter hyperboloid secondary mirror. After figuring and polishing the primary mirror surface and applying a thin nickel barrier, a gold reflecting layer was deposited and protected with a dielectric overcoat [16]. By producing an optical quality surface on the beryllium, only minimal nickel and gold layers were required, thereby avoiding the thermal distortion that had been seen in the MIRIS/IRIS mirror. The secondary mirror is less susceptible to thermal distortion and was therefore nickel electroplated and polished before applying the gold surface. After 19 years in space no degradation in telescope performance has been found, indicating that the mirror coatings and figure have not changed measurably. This coating technology, pioneered by CIRS, was subsequently used on the James Webb Space Telescope [17].

The secondary mirror is mounted at the end of a 33 cm length, 7.8 cm diameter tube that is attached to a flange at the center of the primary mirror. Three fins support the secondary mirror at the end of the mounting tube. Light from the primary passes the fins to reach the secondary and is then sent down the interior of the tube, at f/6, to the focal plane of the telescope. At the telescope focal plane, 11.6 cm behind the primary, the beam passes through a field mask that blocks stray light. The image plane is then field-divided at a roof-shaped mirror that directs separate beams to the mid-infrared and far-infrared portions of the spectrometer. Because the detectors are smaller in the mid-infrared and, therefore, the image quality must be higher there, optical aberrations were minimized by placing the telescope axis at

Table 1. CIRS Instrument Parameters

Type of spectrometer:	FTS
Telescope Diameter (cm):	50.8
Total spectral range (cm^{-1}):	10 to 1500
Spectral resolution (cm^{-1})*:	0.5, 1, 3 & 15
Scan speed (cm/s):	0.0208
Scan time (s):	2 to 50
Data Telemetry Rate (bits/sec)	4000
Optics Temperature (K)	170
Electronics Temperature (°C)	18-22
FAR-INFRARED	
Polarization Interferometer	
Spectral range (cm^{-1}):	10 - 600
Field of view (mrad)	3.9 diameter
Focal plane:	FP1
Temperature (K)	170
Detectors	Two thermocouples
Detector diameter (μm):	1000
Peak D* (cm $Hz^{1/2}$ W^{-1})	4×10^{9}
NEP (W)	3×10^{-10}
MID-INFRARED	
Michelson Interferometer	
Spectral range (cm^{-1}):	580 -1500
Detector temperature (K)	76-87
Detector arrays	two each 1 x 10
Detector size (μm)	200 square
Detector spacing (μm)	215
Detector IFOV (mrad)	0.27 square
IFOV spacing (mrad)	0.29
Focal plane:	FP3
Spectral range (cm^{-1}):	580 -1100
Detector type	PC HgCdTe
Peak D* (cm $Hz^{1/2}$ W^{-1})	2×10^{10}
NEP (W)	1×10^{-11}
Focal plane:	FP4
Spectral range (cm^{-1}):	1050 -1500
Detector type	PV HgCdTe
Peak D* (cm $hz^{1/2}$ W^{-1})	4.5×10^{11}
NEP (W)	4×10^{-13}

*Apodized, see text

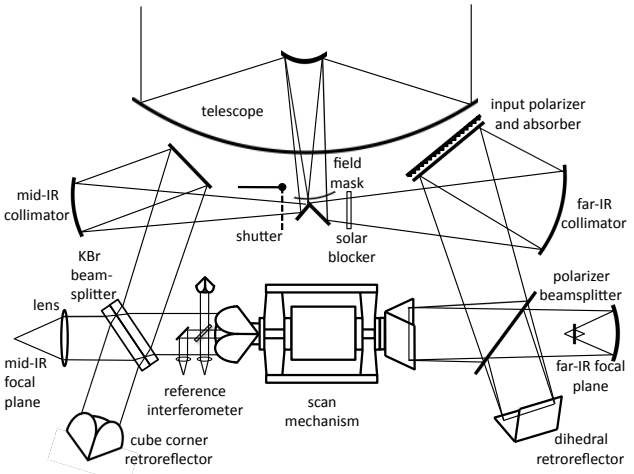

Fig. 3. CIRS conceptual diagram. Two interferometers, mid-infrared and far-infrared, share a telescope and a scanning mechanism. A reference interferometer is inserted into the mid-infrared beam in front of the moving retroreflector. Calibration is accomplished with reference to views of deep space and views of the closed shutter.

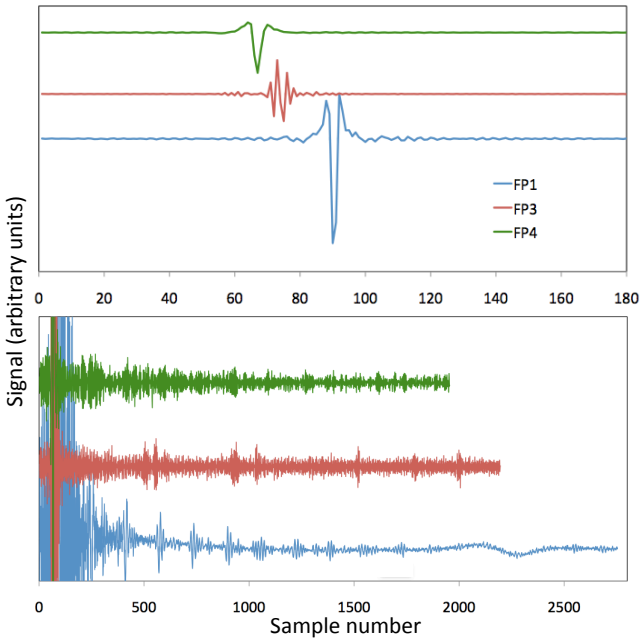

Fig. 4. Examples of interferograms from the far-infrared (FP1) and mid-infrared (FP3, FP4) in CIRS. All three are filtered for noise spikes and data quality. In the upper panel only the portion of each interferogram around zero–path difference is shown. In the lower panel the full interferograms are shown with the intensity scale expanded. The interferograms, which correspond to 0.5 cm^{-1} resolution spectra, were scanned in 50 seconds. Differences in lengths are due to the way sampling is performed in the three focal planes. The slowly varying baseline in FP1 is a repeatable electrical artifact. All three interferograms were recorded on Saturn in 2011-13 and are large averages of data.

the mid-point between the two mid-infrared fields of view. The far-infrared field is thus offset as shown in Fig. 6. We adjusted the position of the telescope field mask during testing to avoid vignetting of the mid-infrared image.

To provide some shielding against solar heating of the primary mirror, a sunshade baffle was placed around its outer rim. The sunshade is isolated from the primary mirror except at its mount at the center of the back of the mirror. The sunshade surrounds the back and sides of the primary and blocks sunlight from the primary when the sun is more than 77° from the instrument boresight. Sunlight is permitted on the primary during operation, but the combination of its reflecting surface and the sunshade allows the temperature of the primary to be controlled at 170±0.1 K. A baffle, also made of beryllium, surrounds the secondary and its mount at the end of its mounting tube. Flight rules require the sun to be kept 15° degrees from the telescope boresight for thermal stability and 5° for damage avoidance. The focus of the telescope was adjusted for optimum performance at 170K. At the telescope focal plane 80% of the energy from a point source at 632.8 nm wavelength fell within a 207 μm diameter, corresponding to 0.15 mrad on the sky. Since this spot size is smaller than the CIRS detector sizes in both the far- and mid-infrared, image resolution was limited by the detector size and diffraction limit. The error in locating the boresight of the telescope was required to be less than ±0.06 mrad to control its contribution to the overall 1-mrad boresight tolerance of the instrument. In flight, the boresight of CIRS, defined as the center between the mid-infrared focal planes, was measured by scanning Jupiter and was found to be offset from the nominal spacecraft pointing by 1.7 mrad away from the spacecraft body (spacecraft +X direction) and 0.04 mrad toward the high-gain antenna (spacecraft –Z direction). A deployable cover protected the telescope on the ground and in flight. The cover was designed to prevent contamination

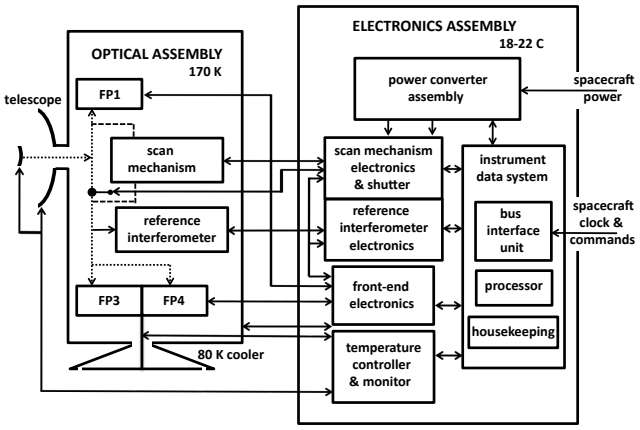

Fig. 5. Block diagram of CIRS. The electronics assembly contains all warm electronics boards and provides power, operational control, signal handling, data processing and temperature control for the instrument. The optics assembly (170 K and 80 K) contains the detectors and preamplifiers, the scan mechanism and the reference interferometer. Data, control and power paths are indicated with arrows.

and to block sunlight when the spacecraft was in the inner solar system. FP1, the far-infrared focal plane, was especially vulnerable to damage from direct solar exposure. Having a conical shape, the beryllium cover (Fig. 1) formed a seal at the rim of the primary sunshade and tapered to a close-fit around the outside of the secondary baffle. A wax-actuator mechanism with built-in redundancy, located at the apex of the cover on the secondary baffle, was activated to deploy the cover. Originally the plan was to eject the cover just prior to arrival at Saturn. However, when the mission obtained approval for science operations at Jupiter we analyzed the possibility of an accidental exposure and decided to accept the risk. The cover was removed on 20 September 2000, just before the Jupiter encounter.

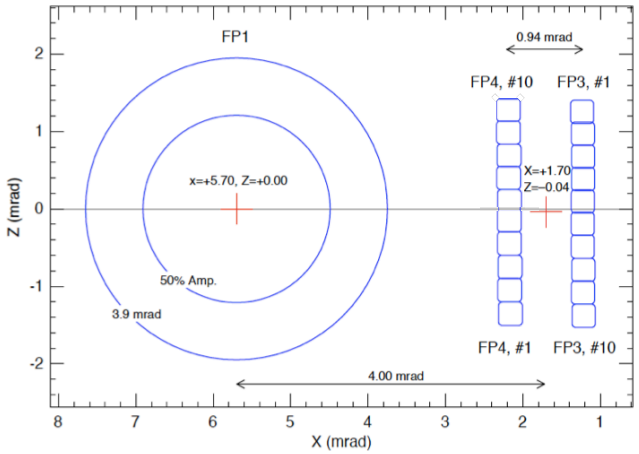

Fig. 6. CIRS fields-of-view measured using bright stars and raster scans of Jupiter just prior to reaching Saturn. The X, Y-origin is the nominal spacecraft pointing axis. The CIRS telescope axis is offset by X=+1.70 and Y=-0.04 mrad. The physical diameter of FP1 is 3.9 mrad, but the half-peak (50% Amp.) response is measured to be 2.5 mrad. Small deviations in position of FP3 and FP4 detectors are within the measurement accuracy.

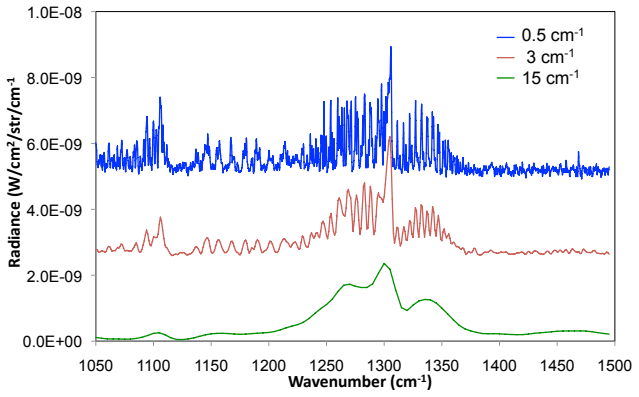

Fig. 7. Three resolutions of FP4 spectra on Saturn. These data are averages of spectra selected from the whole disk of Saturn during the time period 2008-12. CIRS resolution is selected by choosing the length of the interferometer scan. Spectra at 0.5 cm^{-1} and 3 cm^{-1} resolution are offset in radiance.

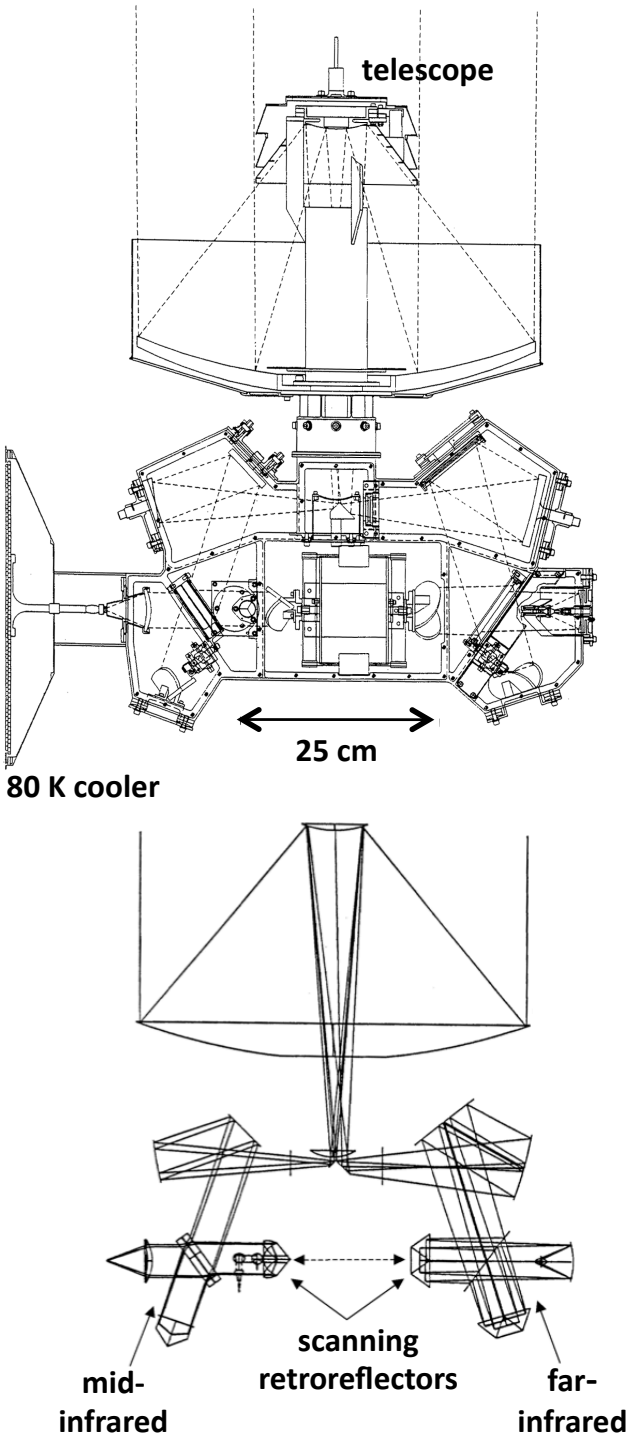

Fig. 8. Mechanical (upper) and optical (lower) layouts of the CIRS instrument. Two interferometers cover the mid-infrared and far-infrared and share both the telescope and the scan mechanism

B. Far-Infrared Interferometer.

The requirement to cover 10-600 cm^{-1} in the far-infrared drove us to choose a polarization interferometer as the spectrometer for that portion of the spectrum. Wire grid polarizers are inherently broad-band in that they have good efficiency at all wavelengths longer than about twice the wire spacing. A drawback is that using only one polarization introduces a loss of half of the incoming radiation and makes the instrument polarization-sensitive. In CIRS wire-grid polarizers served as input polarizer, beamsplitter and output polarizer in the far-infrared interferometer. The polarizers were deposited on 1.5-μm thick mylar pellicle substrates. Individual wires are 2 μm wide and the wire spacing is 4 μm (i.e., a 2 μm gap between wires). In the original CIRS design the polarizers were free-standing wire-grids, but in response to the 1992 descope we changed to substrate-mounted polarizers to recover the spectral region of the lost FP2. Because a substrate permitted smaller wires and narrower spacing, as well as a smoother surface, the shortwave limit of the polarizer was extended to 600 cm^{-1}. Mylar has spectral features in the far-infrared, but they do not appear in spectra after calibration.

The far-infrared optics have been described by Crooke and Hagopian [18, 19]. Optical design of the far-infrared portion of CIRS is shown in Fig. 10. Coming from the field mask and roof mirror, the far-infrared beam first passes through the solar blocker, a filter that transmits only the far-infrared beyond 700 cm^{-1}. The solar blocker protects the far-infrared detector against damage from accidental direct exposure to the sun at Saturn. Beyond the solar blocker the beam is collimated at an off-axis parabolic mirror and then strikes the input polarizer. Its wire grid is rotated from vertical (normal to the page in Fig. 8) such that the portion of the beam that is reflected from the input polarizer toward the beamsplitter is polarized at 45°. The wire grid of the beamsplitter is oriented vertically, so the beam is split into the two arms of the interferometer with the reflected beam polarized vertically and the transmitted beam polarized horizontally. These are sent to dihedral mirror retroreflectors, one of which is fixed in place and the other attached to the scan mechanism. Each dihedral interchanges the horizontal and vertical orientations of the beams and sends them back to the beamsplitter. Switching the polarizations reverses transmission and reflection at the beamsplitter and causes both beams to be sent to the focal plane. Moving the retroreflector changes the difference in optical path between the two beams, which changes the polarization state (ellipticity) of the combined beam. In the FP1 focal plane assembly (Fig. 11, Fig. 12) a parabolic mirror focuses the beam at an output polarizer analyzer. The analyzer wire grid is oriented at 45° and alternately transmits or reflects the beam as the polarization changes. This modulates the signals from two thermocouple detectors that are sensing the transmitted and reflected beams. Because the signals from the two detectors are 180° out of phase, they are wired in series with opposite polarity to double the signal. During the modulation, when each detector is not seeing the input from the telescope, it is instead viewing an absorber

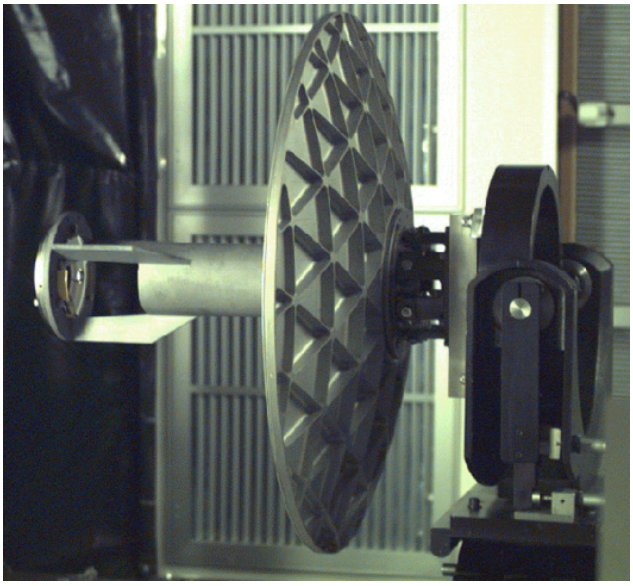

Fig. 9. The CIRS all-beryllium 50.8 cm diameter telescope. Incoming light is focused by the primary mirror onto the secondary mirror (left), which then sends an f/6 beam to the image plane located 11.6 cm behind the primary (right). An aluminum tube in the form of cut-out fingers makes the transition from the beryllium telescope to the aluminum optics housing.

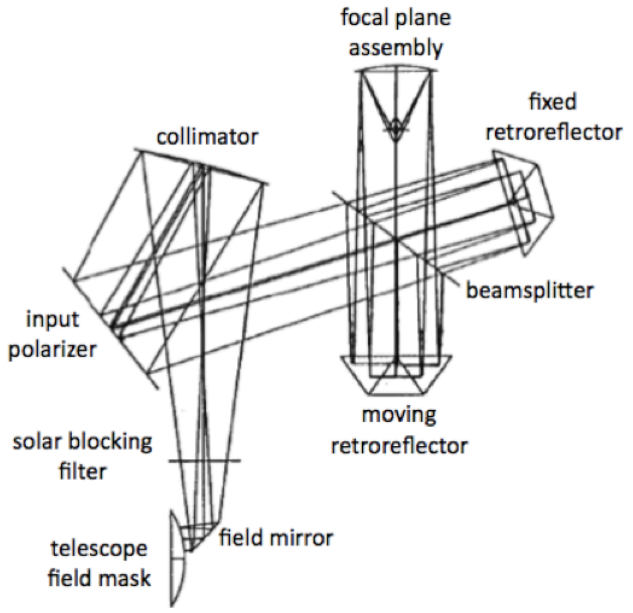

Fig. 10. Optical diagram of the far-infrared section of CIRS. Light from the telescope image (field mask) is sent to a collimating mirror and flat input polarizer and on to the interferometer. A polarization beam splitter splits the beam into two orthogonal components. Dihedral retroreflectors send the beams back to the beamsplitter where they are re-combined. In the focal plane assembly an output polarizer sends modulated light to the thermocouple detectors.

plate located behind the input polarizer. Scanning the retroreflector causes the signal at each detector to alternate between the telescope and the absorber, creating an interferogram (Fig. 4). The absorber has an emissivity of 98.4%. Its temperature, near 170 K, is monitored and used in the radiometric calibration. Within the interferometer the collimated beam has a diameter of 48 mm. The thermocouple detectors are each 1 mm diameter with a Winston cone concentrator accepting an f/1 focused beam from the camera mirror. The detector diameter projects to 3.9 mrad in the field of view (Fig. 6). In-flight mapping showed that the far-infrared field of view sensitivity pattern is approximately Gaussian with a FWHM diameter of 2.5 mrad.

Thermocouple detectors were chosen for the far-infrared because they had the highest sensitivity of any type of detector operating at 170 K. We used Schwarz-type thermocouples made from gold foil attached to p- and n-type bismuth telluride posts. The detectors were developed by the University of Karlsruhe [20]. A gold-black layer coats the gold foil to enhance infrared absorption. At the 0.02 cm/sec scan speed of the retroreflector, modulation on the detectors is in the range 0.4-25 Hz. At these frequencies our thermocouples had detectivities greater than 4×10^9 cm$\sqrt{\text{Hz}}$/W. The signal from the detectors is boosted by a factor of 100 in a transformer and preamplifier that are housed in the warm electronics assembly. The transformer matches the low impedance detectors, about 10 ohms each, to the noise-levels of the preamplifiers. The detector circuit provides redundancy in the event of failure of one of the detectors. With the throw of a latching relay, the circuit switches between series and parallel operation. Series is the nominal mode in which the two out-of-phase detector signals are added. In series mode, failure of one detector would also eliminate the second detector, but by switching to parallel mode the remaining detector could still be used. Although the parallel mode was tested on the ground before launch, it has not been needed in flight.

C. Mid-Infrared Interferometer.

The optical design of the mid-infrared portion of CIRS is shown in Fig. 13 [21]. In the mid-infrared interferometer, the beam coming from the telescope field mask and roof mirror is collimated and sent to the beamsplitter. The dispersion introduced by the beamsplitter substrate is balanced in the compensator by having both transmitted and reflected beams pass through the same thickness of substrate. A layer of germanium on one surface forms the beamsplitter, while anti-reflection and protective coatings are applied to all surfaces of the beamsplitter and compensator. Both beamsplitter and compensator substrates are KBr, and they share a common mount. To eliminate fringing, both substrates are wedged 0.1° and the gap between them is wedged 2°. The beam is divided approximately 50-50% in amplitude and passed to two cube-corner hollow retroreflectors, one of which is attached to the scan mechanism. At the beamsplitter, the return beams are recombined with a phase shift and sent to the interferometer focal plane (Fig. 14). As the moving retroreflector is scanned the phase changes between the two beams and the interference causes the intensity at each detector to be modulated (the combined beam alternates between the detector and the telescope). The detector signal thereby

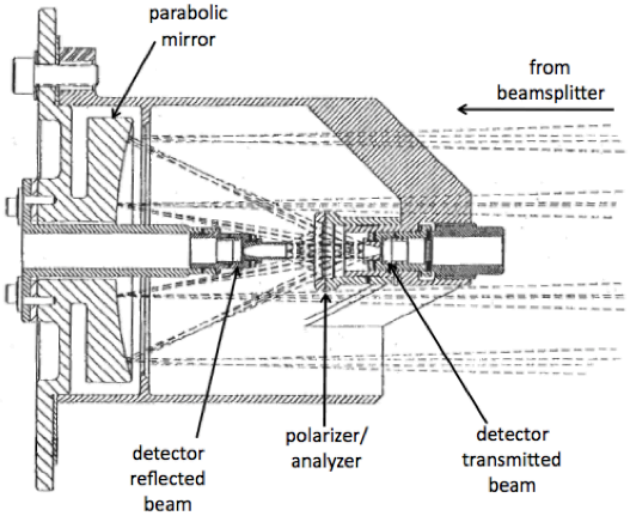

Fig. 11. Diagram of the FP1 assembly for the far-infrared portion of CIRS. Polarization-modulated far-infrared light coming from the beamsplitter is focused on a small polarizer analyzer that passes or transmits the two orthogonal polarization states. Two thermocouples detect the interferogram signals.

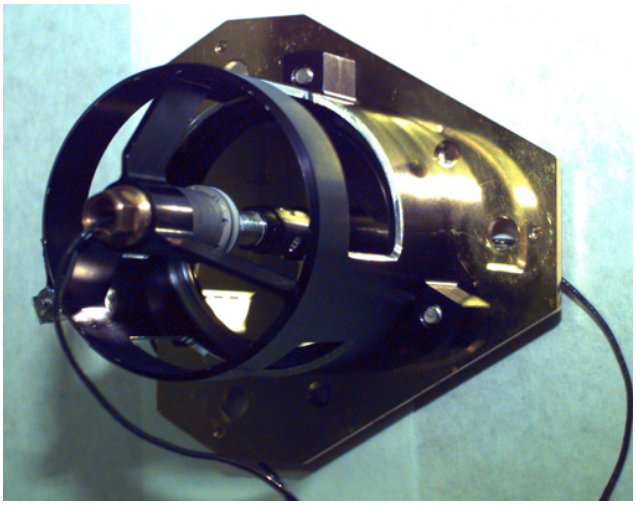

Fig. 12. The FP1 assembly in CIRS. The 48 mm diameter beam is focussed at f/1 onto a polarizer analyzer and then to Winston cone concentrators in front of two thermocouple detectors. A hole and mounting flange on the optics assembly accepts the FP1 assembly. Cut-outs in the cylindrical walls dampen acoustic disturbances during launch.

creates an interferogram (Fig. 4). The beam, which is 45 mm diameter within the mid-infrared interferometer, is focused by a lens at f/1.2 onto the focal plane. The anti-reflection coated germanium lens forms an image at the focal plane where two 10-element HgCdTe linear detector arrays, FP3 and FP4, are mounted. FP3 has a photoconductive array covering 580-1100 cm^{-1}, while FP4 has a photovoltaic array covering 1050-1500 cm^{-1}. Each detector element is 200 μm square. Measurements prelaunch and in-flight show that the

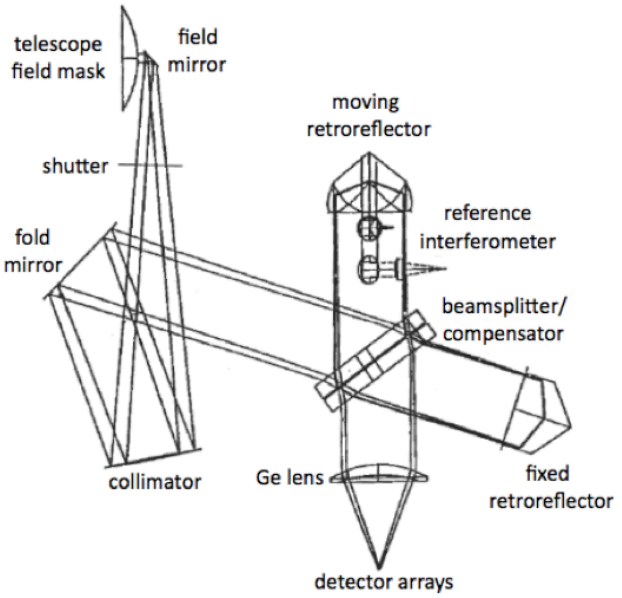

Fig. 13. Optical diagram of the mid-infrared section of CIRS. Light from the telescope image (field mask) is sent to a collimating mirror and fold mirror, which directs the beam to the interferometer, where it is split at a KBr beamsplitter. Cube-corner retroreflectors send the beams back to the beamsplitter for recombining. A lens focuses the modulated light on the HgCdTe detector arrays. The reference interferometer uses the center of the mid-infrared cube-corner.

detectors are each 0.27 mrad FWHM in the telescope field of view and are separated center-to-center by 0.29 mrad [22]. The FP3 and FP4 arrays are attached to the cold finger of a passive radiative cooler described in section 5. The two arrays are aligned with their detectors next to each other and separated center-to-center by 0.68 mm. The photovoltaic detectors were developed by CEA Saclay, France and the photoconductive detectors were developed at Goddard Space Flight Center [23]. Both detector arrays were delivered to the University of Oxford [24], where they were precisely co-aligned, integrated with the lens, focused and boresighted. In the original CIRS design each mid-infrared array was read by 10 amplifier channels. However, the number was reduced to five channels during the 1992 descope. To retain flexibility in observations, a switching circuit apportions the ten detector signals among the five channels in three ways: 1) the 5 channels are toggled between odd and even detectors for observations in which high spatial resolution mapping is desired without moving the spacecraft; 2) adjacent detectors are combined in each of the five channels when full spatial coverage with reduced spatial resolution is required; and 3) the five center detectors are connected to the five output channels for high spatial resolution with reduced spatial coverage. All three of these modes have been used in flight, the most common being odd and even.

D. Reference Interferometer.

The motion of the scanning retroreflectors in CIRS is monitored and controlled by a reference interferometer (Fig. 15). The reference interferometer uses a solid state diode laser (SDL model 5601, containing two lasers) to produce interference fringes that are regularly spaced in optical path difference and are used to control the scan and to trigger data sampling. The reference interferometer has been described by Martino, and Cornwell [25]. We used a laser instead of the neon bulb used in previous IRIS instruments to improve output intensity and reliability. The laser operates at the 170 K optics temperature and emits at 784.5±0.3 nm wavelength. Since the wavenumber scale in CIRS spectra depends on the laser wavelength, we calibrated the wavelength when we reached Jupiter using known, strong lines of atmospheric methane near 1330 cm^{-1} [26]. When the laser changed frequency on occasion later in the mission we repeated the spectral calibration using strong methane lines in Titan's spectrum. This process is reviewed further in section 8.B. A "white light" interference signal is also produced by the reference interferometer. A light emitting diode (LED, Opto-Diode model OD880) with a broad emission spectrum between 800 and 920 nm produces a narrow burst of fringes at zero-path difference (ZPD) of the reference interferometer. The white light ZPD precedes the infrared ZPD by 347 μm and triggers start of data collection. As a result, the beginning of scan is very repeatable, producing consistent sampling and permitting on-board coadding of successive interferograms.

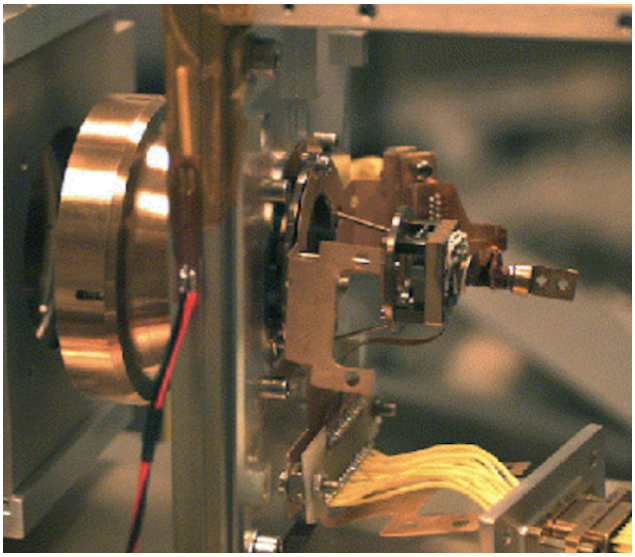

Fig. 14. The CIRS mid-infrared focal plane assembly. Two HgCdTe detector arrays are mounted on a stage that is supported by a tripod of titanium legs (center) attached to the lens assembly (right). A flexible copper strap (right) provides the thermal connection to the cooler cold finger. Infrared light from the beamsplitter (to the left) is focused by a germanium lens (left) onto the focal plane.

In the earliest design of CIRS the reference interferometer beam followed the same path as the mid-infrared, including through the beamsplitter and both cube corner retroreflectors. In principle this would provide optimal tracking of the path difference in the mid-infrared. However, it was realized that from an engineering perspective there were reasons to not share all of the optics with the infrared in CIRS. First, two beamsplitter coatings would be required on

the KBr beamsplitter with one in the center optimized for the short-wavelength reference interferometer. Eliminating the central coating would simplify the beamsplitter and reduce risk. Second, if the scan mechanism could be operated separately from the mid-and far-infrared interferometers, development and testing of the scan mechanism would be greatly simplified. We decided to have a separate reference path sharing only the moving mid-infrared cube-corner (the alternative of placing the reference interferometer on the opposite end of the scan mechanism, as was done in Voyager IRIS, was not an option because that position was occupied by the far-infrared retroreflector). Although using different optical paths for the infrared and reference beams is not ideal, the little relative drift we have seen is corrected during calibration by making a phase adjustment. Since the main requirement of the reference interferometer was to track the motion of the cube-corner retroreflector during scans, we placed the reference interferometer directly in front of the retroreflector. Laser and LED beams are first joined at a polarizing beam combiner and pass through a quarter-wave plate to prevent laser light from returning to the laser. The beam is then inserted into the center of the infrared beam by a fold mirror and sent to the beamsplitter. Fold mirror and beamsplitter reside entirely within the central portion of the telescope beam, i.e., inside the shadow formed by the secondary mirror. The glass cube beamsplitter and a 45° prism mirror are glued into a tube to create a single, stable unit. From the beamsplitter half the beam is transmitted to the scanning retroreflector and half to a small, stationary cube-corner retroreflector. The return beams from the retroreflectors are recombined at the beamsplitter and sent

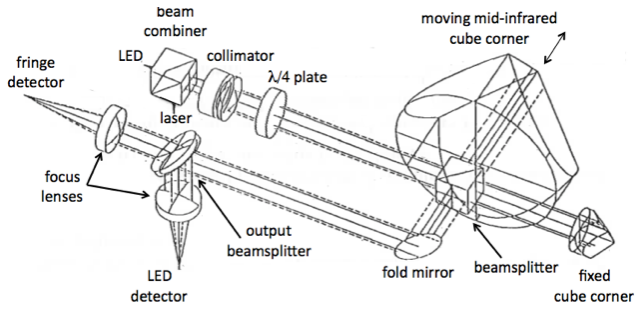

Fig. 15. Reference interferometer optical layout. A solid state laser provides the reference fringes and a light emitting diode creates the broadband "white-light" signal. The reference interferometer measures the motion of the mid-infrared cube corner retroreflector.

to the reference detectors. Another beamsplitter separates beams between the laser and LED detectors. Pinholes are used in front of the detectors to further isolate the laser and LED light. Silicon PIN photodiodes (EG&G model SGS100) are used for both the laser and white light detectors. A pulse train generated by the fringe zero-crossing is sent to the scan mechanism electronics for scan control.

The reference laser has operated flawlessly since the Cassini launch in 1997. We have not needed the backup laser, but we did verify during the mission that it worked. There have been no spectral drifts, except that the laser sometimes changes wavelength mode when it is turned on after an instrument sleep period [27]. Because we know the mode spacing we can easily change the spectral calibration to compensate for mode hops (section 8.B). During the long periods between the times when the instrument is turned off the wavelength is very stable. We have seen a long-term decrease in the laser signal, about 8% over the mission. That may be due, at least in part, to a slight drift in the optical alignment over time. The laser has been used beginning just after launch, during cruise for instrument checks, at Jupiter in 2000-01, and at Saturn since 2004. The total amount of on-time is over thirteen years. Housekeeping information is not available for the LED, but it has shown no signs of deterioration in performance over the mission.

4. MECHANICAL DESCRIPTION

CIRS consists of two principal subsystems, an optics assembly and an electronics assembly (see Fig. 5). The optics assembly contains the telescope, scan mechanism, 80 K cooler and the mid-and far-infrared interferometers. The optics assembly is supported on the spacecraft remote sensing palette (RSP) by a thin-walled titanium tube, which allows the optics assembly to be cooled to 170 K (except for the 80 K cooler and mid-infrared focal plane). Aluminum was used throughout the optics assembly except for the beryllium telescope. The telescope was made of beryllium to take advantage of its thermal uniformity and low thermal expansion. To accommodate the difference in thermal expansion between beryllium and aluminum, a flexible aluminum support makes the transition between the telescope and the optics housing. For ease in machining and to provide surfaces for mounting the various mirrors, the optics housing is designed with a rectangular cross-section, rather than the tubular design used in the previous IRIS instruments. External flat surfaces on the housing serve as mounts for mirrors, far- and mid-infrared focal plane assemblies, reference interferometer components and calibration shutter. External alignment adjustments are made by shimming at the attachment points. Internal optical adjustments are performed with shims or sliding wedge mechanisms with locks. Removable covers allowed access to the interior optical components during integration and testing. Polarizers in the far-infrared, and beamsplitter and compensator in the mid-infrared, are held with springs against precision surfaces in their mounts.

CIRS has two mechanisms, a scan mechanism and a calibration shutter. The design of the shutter was adapted from DIRBE on COBE [28]. The shutter consists of a mirror mounted on an arm that is pulled into the mid-infrared beam by an electromagnet. A failure of the electromagnet would leave the shutter in the open position, thereby allowing the instrument to continue to operate. During ground testing and in flight the calibration shutter has performed flawlessly. The calibration shutter is described further in section 7.

We based the CIRS scan mechanism on Voyager IRIS, but the CIRS design needed to increase the scan length to 11 mm from the 1.6 mm of IRIS. The CIRS scan mechanism is shown in Fig. 16. It is described in detail by Hakun and Blumenstock [29]. A prototype of the CIRS scan mechanism was described by Michel and Courtin [30]. The scan mechanism mass is 1.8

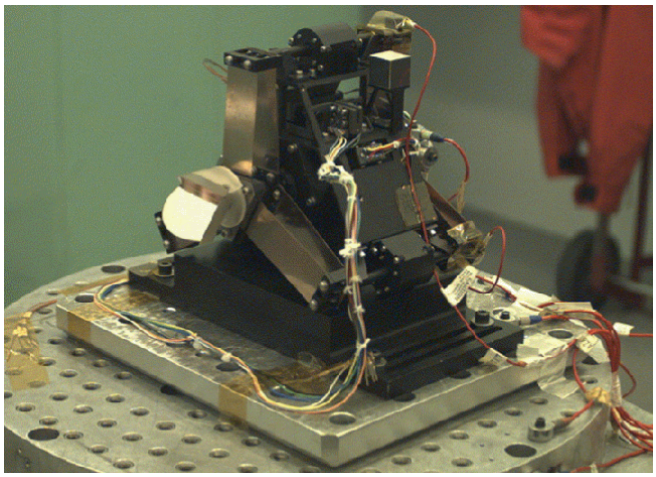

Fig. 16. CIRS scan mechanism (engineering unit) prepared for vibration testing. Paired leaf springs, each consisting of three blades, support a central moving shaft with a maximum linear travel of 1.4 cm. A cube corner retroreflector is mounted on the moving shaft. The scan motion is along the axis of the cube-corner and perpendicular to the planes of the leaf springs.

kg and it is approximately 15 cm across. The mechanism is based on leaf flexures arranged in a symmetrical three-leaf pattern. At each end of the mechanism a flexure leaf makes the transition from the fixed mechanism body to one of three intermediate "outrigger" rods, and another leaf makes the transition from the rod to the moving shaft. The leaves are stiff enough to keep the shaft from sagging appreciably during testing in 1 g. As the shaft moves all leaves bend, so that the rods "breathe" in unison, and the shaft travels in a straight line. Scaling the scan length up from IRIS presented some challenges. One difficulty was that the leaf flexures needed to be longer in order to achieve the scan length and avoid over-stress that would distort the springs. But increasing the length decreased the leaf stiffness. With beryllium-copper as the material, an optimum length for the flexure arms is 8.7 cm, giving a 1.1 cm travel during the interferogram scan and 1.4 cm travel to the end limits. To avoid wobble at the center of travel where the leaf springs are in a neutral position, care was taken in matching and aligning the leaves during assembly. Vibration of the arms during launch and operation was minimized with passive eddy-current dampers on the outrigger rods.

Cube-corner and dihedral retroreflectors are attached to the ends of the tube-like scanning shaft [31]. Maximum tilt during motion was measured before launch to be ±2 arcsec and shear was less than 18 μm. A linear motor moves the shaft. The permanent magnets of the motor are placed on the moving shaft to eliminate heat conduction through wires. A wire bobbin provides the changing magnetic field during scanning. With the bobbin fixed in place, problems with moving wires are avoided. Differential eddy current modulation in a rod located inside the bobbin gives a measure of displacement. This provides coarse scan control as an alternative to the reference interferometer. Scan motion is controlled by an electronics board located in the electronics assembly [1]. During data-taking, fine control is maintained by locking a pulse train from the reference interferometer to pulses generated by a stable oscillator. With the scan velocity of 0.0208 cm/sec, digital pulses formed from the zero-crossings of the laser fringes occur at 1066 Hz. Scan rate is controlled to better than 1%. During flyback following each scan the mechanism is out of lock and moves at about 0.5 cm/sec. For launch the shaft was driven to one end of travel and secured with a yoke on a locking mechanism. Unlocking took place one week after launch. The mechanism is operated most of the time, even when not taking data, to minimize temperature variations.

5. TEMPERATURE CONTROL

CIRS has four temperature zones, each with its own thermal operating range and control. These zones are the: 1) optics assembly; 2) telescope; 3) 80 K cooler and focal plane; and 4) warm electronics. Multi-layer insulation covers all surfaces except for the 170 K radiator, the 80 K cooler annulus and cold patch, and the telescope aperture. The warm electronics assembly is connected to the cold optics assembly by a thermally isolated harness that accommodates the ~125 K drop between the two assemblies. Thermistor sensors are used in the optics assembly, silicon diodes were used in the telescope and 80 K focal plane, and a platinum resistance thermometer (PRT) is used on the 80 K cooler cold patch. The optics assembly is cooled to 170 K with a thermal radiator consisting of two walls of the housing exposed to space. Temperatures are monitored with thermistor sensors at a variety of locations in the assembly, including a thermistor near the radiator panel heater for temperature control. Another thermistor, attached to the absorber on the far-infrared input polarizer, is used for calibration of FP1 spectra. Proportional and derivative feedback control of the heater current keeps the temperature of the optics assembly within 170±0.1 K. The telescope is also kept at 170 K, but controlled separately from the optics assembly because the transition mount between the telescope and the optics assembly reduces the thermal exchange between the two regions. In addition, the telescope's two mirrors, primary and secondary, are controlled independently. Both are kept at 170±0.1 K with heaters and proportional feedback circuits. Thermistors on the mirrors provide monitoring and temperature control. Monitoring the telescope sunshade and secondary baffle helps maintain a uniform temperature. Before launch the PRT located on the 80 K cooler cold patch failed, most likely due to a broken electrical contact. Since it was not needed for temperature control, and to avoid risk, a decision was made to fly without repairing the sensor. However, during a Titan flyby in October 2006 the sensor suddenly returned to full operation. It has worked normally during the remainder of the mission. CIRS was allocated 9 W of power for thermal control. Near the end of the mission the heater power came very close to this limit, but fortunately did not exceed it. A lesson learned from this experience is that an instrument should not be limited to the pre-launch power allocation in case it is found that more power is needed in flight. Extra power sometimes becomes available in-flight.

Our choice of HgCdTe detectors for the mid-infrared made it necessary to cool that focal plane to temperatures below 80 K. A passive radiative cooler was developed for the mid-

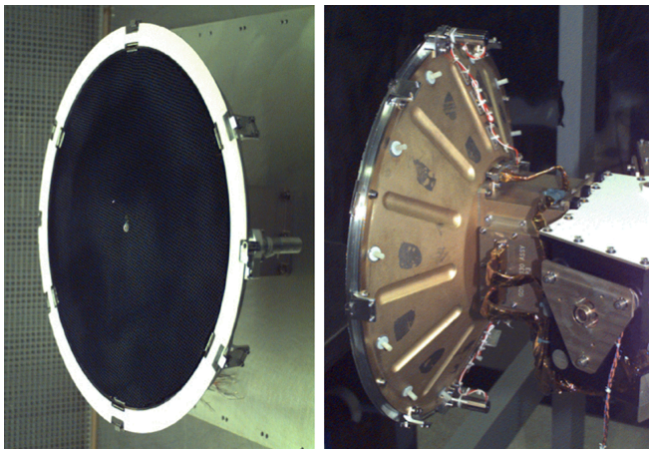

Fig. 17. The CIRS 80 K cooler cools the mid-infrared focal plane in the range 75-85 K. Left panel: The cold patch is black-painted honeycomb. The white annulus radiator cools the housing rim to about 130 K. A cover release actuator is attached to the outer rim. Right panel: The titanium housing supports the cold patch and surrounds the focal plane. Cables connect to the focal plane electronics. At right the back of the cube-corner mount can be seen attached to the outside of the main optics assembly.

infrared by the University of Oxford [24]. The cooler is shown in Fig. 17. This 80 K cooler maintains the detectors at their operating temperature by radiating to space. The cooler generally keeps the detectors near 76 K, but occasionally when solar or planetary heating cannot be avoided the temperature rises above 80 K. Focal plane temperature is controlled to one of a series of setpoints so that the temperature can be kept stable during observations. The cooler cold patch is a 40 cm diameter radiator disk aimed away from the spacecraft toward deep space (along the spacecraft +X axis). The cold patch was protected on the ground and during early cruise by a spring-deployable cover that was released in April 2000 prior to arrival at Jupiter. The cold patch surface is an aluminum honeycomb coated with conductive black paint for maximum thermal emissivity. The cold patch is suspended by stainless steel wires from a titanium ring that in turn is attached to the rim of a titanium support housing. An aluminum annulus with high thermal emissivity covers the rim of the housing and acts as a secondary radiator to cool the rim. Except for the annulus, multi-layer insulation covers the cooler housing. A cold finger is attached to the inside center of the cold patch and connects via a flexible multi-layer copper foil strap to the focal plane mount (Fig. 14). The two 10-element detector arrays are bonded onto carriers that are attached onto the mount with screws and positioned using dowels against reference surfaces. The cold focal plane mount is attached to the lens assembly by a thermal isolator in the form of a tripod made of legs of titanium alloy. Cold (170 K) front-end preamplifier electronics for both FP3 and FP4 are mounted in the housing adjacent to the focal planes to minimize the cable lengths. Following testing at Oxford [22] the full assembly (cooler plus FP3 & 4) was delivered as a unit to Goddard Space Flight Center for integration with the CIRS optics assembly.

Survival heaters on the optics assembly and 80 K cooler are activated by the spacecraft when the instrument is off. Decontamination heaters can also be operated by the spacecraft while CIRS is in off mode. The decontamination heaters have been turned on twice during the mission, once prior to mechanism latch release and again just before ejection of the telescope cover. The heaters warmed the wax actuators and drove contaminants onto the cover. Throughout the mission there has never been any evidence of contamination.

6. ELECTRONICS/OPERATIONAL MODES

The electronics assembly, housing the warm electronics boards (see Fig. 5), is mounted directly to the spacecraft remote sensing palette. Circuit boards in the electronics assembly include a power converter assembly (PCA), scan mechanism electronics (SME) and reference interferometer electronics (RIE), an optics temperature controller/monitor (TCM), front-end electronics (FEE) and the instrument data system (IDS). The PCA, comprising four boards, converts the primary 30 V spacecraft bus power for secondary subsystems requiring ±15 V, ±12 V and +5 V. The PCA also operated the cover releases for cooler and telescope. The SME controls the scan mechanism and operates the calibration shutter. The RIE provides a pulse comb for scan mechanism velocity control and for triggering data sampling. The TCM stabilizes the FP3/FP4 focal plane temperature at commandable setpoints between 75 K and 87 K. The TCM also maintains a uniform 170 K in the optics assembly. The FEE provides conditioning, amplification and digitization of the infrared detector signals. The IDS is a microprocessor that controls all functionality of the instrument, accepts commands, processes data and provides telemetry. The electronics temperature varied during the mission as the solar distance increased, changing from about 22 °C at Jupiter to about 18 °C at Saturn. Preamplifiers for FP3 and FP4 and for the reference interferometer detectors are housed in the 170 K optics assembly.

CIRS has five operating modes: Pre-Sleep, Sleep, Operational, Initialization, and Science. The various modes are described in Fig. 18, along with their approximate power consumptions. From Off the instrument transitions to Pre-Sleep mode in which the PCA, IDS and TCM are on and flight software is loaded. The scan mechanism launch lock was unlatched in Pre-Sleep mode. Safety watchdog commands can transition any mode (except Off) into Pre-Sleep. When a software load is completed and has been validated in Pre-Sleep, a transition is automatically initiated and the IDS flight software reinitializes itself as it switches to Sleep mode. In Sleep the PCA, IDS and TCM are on and the mid-infrared focal plane temperature is set. Sleep mode serves as the standby mode of the instrument and from Sleep any other mode can be reached. The purpose of Initialization mode is to allow the telescope and cooler cover releases to proceed without extraneous instrument operations and power usage. Initialization mode has only been used during cover releases. In Initialization mode PCA, IDS and TCM can be on or off. In Operational mode engineering data and diagnostics can be run, but no science data can be produced. PCA, IDS and TCM are on in Operational mode and the scan mechanism, reference interferometer and front-end electronics are

normally on. In Science mode all electronics are turned on and science data may be recorded (engineering data cannot be collected). Housekeeping data is transmitted in all modes (except Off). In any mode, in the case of a spacecraft safing event, the electronics are turned off in stages to protect the instrument.

Data rate and volume are minimized by optimally sampling the detectors. All eleven detector signals are initially sampled at 1066 Hz, corresponding to every zero-crossing of the laser fringe signal. The signals are electrically filtered to limit their bandwidths. Focal planes 3 and 4, which are aliased in 2nd and 3rd order, are further bandwidth-limited by numerical filtering. Numerical filtering is also applied to FP1. The 1066 Hz rate is reduced by under-sampling in all three focal planes. The final under-sampling factors are 18, 22.5, and 25 for focal planes 1, 3 and 4, respectively. Data volume is also minimized by spatial averaging using detector pairing, by tailoring spectral resolution, and by onboard coadding of successive interferograms. In planning observations it must be kept in mind that each of these types of observation requires its own reference data, recorded in the same manner, for calibration.

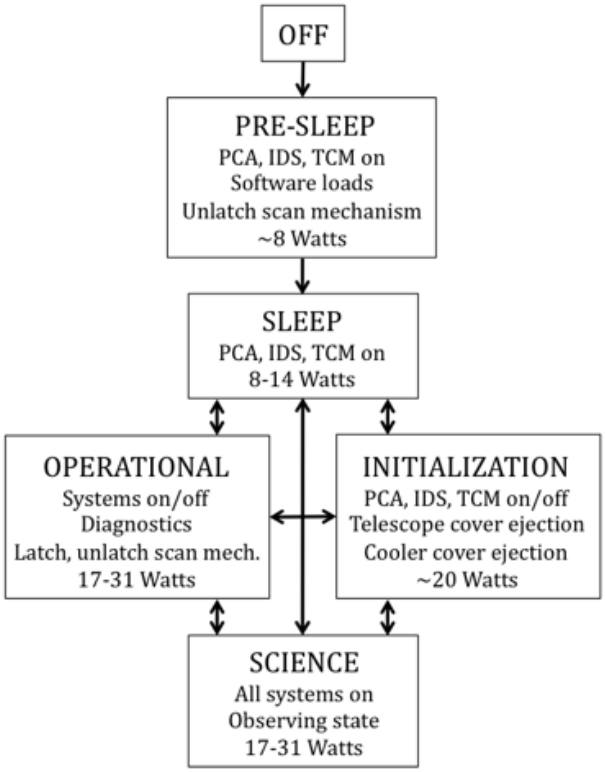

Fig. 18. CIRS operational modes. Use of multiple modes permits efficient management of power consumption and allows the Science mode to be dedicated to data taking. Engineering data are recorded in Operational mode. Sleep mode serves as the standby mode in which power is minimized. Operational mode permits engineering functions and diagnostics to take place without recording science data.

7. RADIOMETRIC CALIBRATION

CIRS is calibrated by comparing with reference sources of known temperatures. The procedure is different for the far-infrared and mid-infrared. In the far-infrared all of the optics, housing and focal plane are at the same 170 K temperature. Calibration with uniform temperature requires only one reference blackbody. The condition of uniform temperature is similar to that of Voyager IRIS [7, 10], with one important difference. Since in CIRS the interferometer is a polarization modulator, during a scan the input is either reflected or transmitted at the input polarizer. Reflection at the polarizer views the sky through the telescope, while transmission gives a view of the 170 K absorber behind the polarizer. The absorber is a black honeycomb with emissivity close to unity. Since it is surrounded by surfaces all at 170K, radiance from the absorber is effectively blackbody emission at 170K. Observing deep space, away from sources in the Saturn system, is therefore equivalent to viewing a blackbody at 170 K but inverted in modulation phase. Deep space interferograms, I_{ds}, are thus used to derive the response

$$R(v) = \frac{FT(-I_{ds})}{B(170\,\mathrm{K})} \qquad (1)$$

where FT is the Fourier transform. Here v is the wavenumber and B is the blackbody radiance spectrum, or Planck, function for 170 K. Writing I_t for the interferogram from viewing a target, the calibrated spectrum from FP1 is

$$S_t(v) = \frac{FT(I_t - I_{ds})}{R(v)} \qquad (2)$$

In the mid-infrared there are two temperature zones. The optics module is at 170 K and in addition the mid-infrared has an 80 K focal plane. Views of two reference sources, one warm and one cold, are required to obtain the response [10]. For the cold reference CIRS observes deep space, which corresponds to a source essentially at 0 K. For the warm reference CIRS observes the 170 K inside wall of the optics housing. A calibration mirror shutter diverts the view toward the interior wall. The shutter is located between the telescope focal plane and the mid-infrared collimating mirror. A sensor provides the temperature of the wall at the shutter view location. The temperature of the housing varies by <0.02 K during an ~1 hour observing sequence and by <0.1 K over long terms. We assume that viewing the housing wall is effectively looking at a blackbody at the sensor temperature with unit emissivity. This is justified because the shutter is effectively viewing the inside of a 170 K cavity. To calibrate the mid-infrared, interferograms of deep space I_{ds} and shutter I_s are recorded at times adjacent to target interferograms I_t. Because the responses and noise of the FP3 and FP4 detectors depend on temperature, the target, deep space and shutter interferograms must be recorded at the same focal plane temperature, or a correction must be applied. The responses of FP3 and FP4 are found from

$$R(v) = \frac{FT(I_s - I_{ds})}{B(170\ \mathrm{K})} \quad (3)$$

and the calibrated spectra are calculated as

$$S_t(v) = \frac{FT(I_t - I_{ds})}{R(v)} \quad (4)$$

Our technique of subtracting deep space from target interferograms before performing the Fourier transform removes the effect of the instrument background, including phase, from the target data [27, 32]. This approach presumes that the instrument phase, particularly the ZPD position, is the same for I_t, I_{ds} and I_s. In those cases in which this is not true we introduce a linear phase shift to the interferogram before subtraction.

Because their responses are different, interferograms from each of the twenty mid-infrared and one far-infrared detectors must be calibrated separately. Deep space and shutter reference data are recorded for every detector. Because the shapes of the interferograms vary slightly with scan length, reference data are recorded for each spectral resolution. In addition, reference data are taken for every detector configuration, evens, odds, pairs and centers, and also in coadd mode. Before recorded interferograms are calibrated they are subjected to a rigorous quality control in which badly distorted interferograms are rejected, and corrections are applied to eliminate interference in the form of noise spikes or spurious modulation. A database of filtered interferograms is created that serves as input to the calibration pipeline. In the calibration pipeline calibrated spectra $S_t(v)$ are calculated for each target spectrum. Both apodized and unapodized spectra are created. Apodization is applied with a Hamming window function. The appearance of line structure in the 615-650 cm^{-1} band of methylacetylene (CH_3CCH) in the unapodized spectrum in Fig. 19 demonstrates the value of archiving both apodized and unapodized calibrated spectra. The most commonly used unapodized resolutions available from CIRS are 0.3, 0.5, 1.5 and 8 cm^{-1}.

The first step in the calibration process is to create averages of reference interferograms, i.e., deep space and shutter-closed. We have two approaches for creating these reference averages, depending on whether we wish to optimize the absolute accuracy of the spectra or maximize the sensitivity to weak spectral features. The goals of these two approaches are not always compatible. For best absolute accuracy the deep space and shutter-closed interferograms should come from the same observation sequence as the target interferograms, or from time periods immediately before or after the target observation [33]. This minimizes changes in the instrument between target and reference data, principally in temperature and zero-path difference. The dataset commonly delivered to NASA's Planetary Data System (PDS) during most of the mission is calibrated with these adjacent reference averages. We have called it the "local calibration". When sensitivity is the goal, however, there are often not enough reference interferograms available from times near the target observation. The number of deep space and shutter-closed spectra must be large enough so that their noise contributions are smaller than the noise in the target spectra. Overall, CIRS collects enough deep space and shutter-closed data to satisfy this requirement. The result is that the signal-to-noise in the averaged spectrum is improved, so that weak spectral features can more readily be detected. However, the absolute accuracy of the calibrated radiance often worsens as the time between target and reference scans increases. When the reference interferograms are not

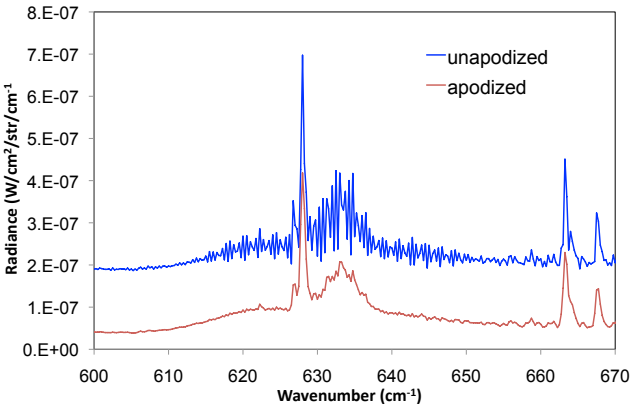

Fig. 19. A portion of the Titan spectrum showing the effect of apodization. The two spectra are from the same averaged high resolution interferogram. Without apodization (blue, offset in radiance) the spectral resolution is 0.3 cm^{-1}, while after applying Hamming apodization the resolution is 0.5 cm^{-1}. The most obvious effect is in the 615-650 cm^{-1} band of CH_3CCH where the line structure is resolved in the unapodized spectrum. Other molecular emissions seen here are from C_4H_2 at 628 cm^{-1}, HC_3N at 663 cm^{-1} and CO_2 at 667 cm^{-1}.

recorded under the same instrument conditions (mostly due to temperature drifts) phase errors can arise. Ordinarily, if the phases of the target and reference interferograms are the same the differences will cancel. However, when we find mismatches between target and reference phases we adjust the phases before subtracting interferograms. Since the errors most often manifest themselves as shifts in zero-path difference, the phase correction is linear. Shifts in zero-path difference are predominantly less than 2 microns. We maintain two types of databases calibrated with these large reference averages (in addition to the local calibration database). One of these, called "global calibration," uses deep space and shutter-closed data from periods separated days or weeks from the target observations. The number of deep space scans is typically several thousand and these are corrected for differences in phase and instrument temperature between target and reference times. The other, called "grand average calibration," uses as large a number of deep space and shutter-closed data as possible over the whole mission (typically more than 30,000 deep space and several thousand shutter-closed). Investigators can choose the calibration dataset that is optimum for their science goals. The global calibration is best for most applications and will be archived in the PDS at the end of the mission. But in cases where the user wishes to have the same reference spectra for

averages of target data taken over a long time period the grand average calibration may be preferred.

8. IN-FLIGHT OPERATIONS AND TROUBLESHOOTING

Under Cassini's distributed approach to operations, the CIRS science team is responsible for all aspects of instrument operations. CIRS operations begin with the science objectives, proceed through observation planning, implementation and instrument commanding, and end with calibration and archiving of the data. The instrument has executed more than 1.4 million commands since April 2001. Aside from a command error in October 2004, no command problems have occurred in the mission. Maintaining the quality of the data while managing the large rate and volume of data has been challenging. To date 166 million raw CIRS interferograms have been collected: 11 million on Titan, 29 million on Saturn, 39 million on the rings, 7 million on icy satellites, and 80 million deep space and shutter. 98% of the observational data have been successfully calibrated. The CIRS investigation provides a full database, both raw interferograms and calibrated spectra, to the scientific community via the PDS. We continue to make small improvements and modifications to our ground system. Flight software updates were most recently uplinked to the spacecraft in June 2014. More changes are in store for the last phase of the mission when proximal orbits will expose Cassini and CIRS to new thermal environment near Saturn and the rings near periapsis.

Collection of deep space calibration data in all modes and focal plane temperatures are performed when CIRS is not pointed at a target, most often during downlinks of data from the spacecraft to Earth. During downlink the spacecraft is often rolling and in these periods we must avoid disturbances caused by the spacecraft reaction wheels. Changes in instrument temperature also complicate the use of deep space data for calibration. Electrical disturbances in the instrument and spacecraft present other limits to the quality of the CIRS data. Here we describe the most important types of trouble and how we deal with them.

A. BIU anomalies.

Occasional flaws in communication between the spacecraft bus and CIRS result in loss of interaction with the spacecraft and shutdown of the instrument. During these periods observation and housekeeping data may be lost. Eight of these bus interface unit (BIU) upsets have occurred, with the last event in April 2014. The BIU errors are believed to be caused by faulty message timing. Changes to the flight software, more frequent checks of the BIU and CIRS memory, in addition to autonomous diagnoses and memory corrections have reduced the rate of occurrence of these shutdowns.

B. Laser wavelength changes.

About fifteen times during the mission, when CIRS has been turned back on following a transition of the instrument to off or pre-sleep states, the reference laser has changed wavelength. This has generally occurred following 1) a BIU anomaly, 2) an instrument flight software load or 3) a spacecraft safing event. Laser changes appear in Fig. 20 as sudden, large jumps or drops in the reference interferometer signal [33]. Changes are infrequent, with the laser usually remaining stable for a year or more, but some events have been separated by only weeks or months. A change is usually accompanied by a recovery period of several weeks. Over that time the laser is predominantly in a single laser wavelength mode, but exhibits some ringing due to mixing with a weaker adjacent mode. During the recovery the weaker mode gradually dies away. As the laser recovers, the principal wavelength does not change enough to affect the calibration. For calibration, the new wavelength must be determined by measuring the positions of known molecular lines. We use emission lines of methane near 1330 cm^{-1} that appear in spectra of Titan. The error in this determination is estimated to be less than 0.01 cm^{-1} at 1300 cm^{-1}. Over the mission the laser has operated at wavelengths of 784.2377+Nx0.1534 nm, where N=0, 1, 2, 3, 4 and 5. Thus the laser operated in one of a series of modes spaced by 0.15 nm. Changes tended to be toward shorter wavelengths as the mission progressed (N=5 occurred in 2006 and N=0 occurred in 2015). This possibly indicates a long-term trend in laser behavior. Also, a long-term decrease in laser signal of about 8% from 2004 to 2016 can be seen in Fig. 20 which may have been due to optical changes not related to the laser operation. After correcting the laser wavelength it is entered into the calibration pipeline and used until the next laser shift. Once the new laser wavelength has been determined it can be applied retroactively and therefore very little data has been lost during the mission because of laser shifts.

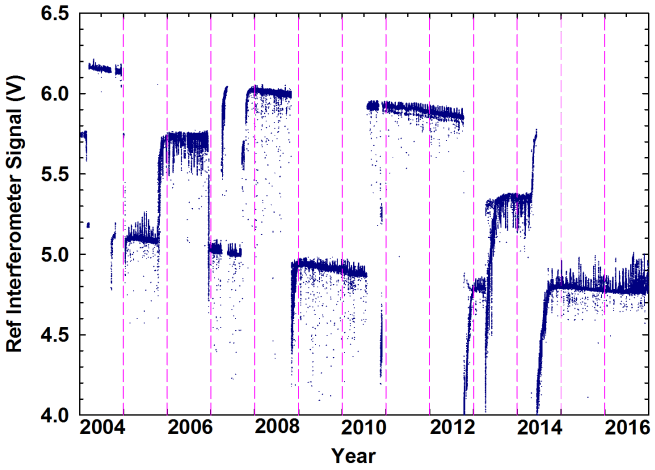

Fig. 20. Signal level from the laser detector in the CIRS reference interferometer during the Saturn tour. The laser signal was typically stable for periods of years, but occasionally changed when recovering from an off state of the instrument. Abrupt changes in signal corresponded to laser wavelength changes. The signal voltages were measured 3 seconds after start of scan.

C. Noise spikes.

During the first instrument check-out after launch we discovered a pattern of noise that had not been seen during ground testing. On the ground this noise had been masked by ambient noise. The main components of the pattern are two regular series of spikes in the interferograms, one series spaced by 8 Hz and the other spaced by 0.5 Hz. These are seen

in FP1 and FP3 but not in FP4. The 8 Hz spikes are synchronized with the spacecraft clock and correspond to real-time interrupts from the BIU or to operations in the CIRS data computer that occur at the clock rate. Interferogram scanning is also locked to the spacecraft clock and is therefore synchronized with the 8 Hz spikes. The 0.5 Hz spikes occur when CIRS sends data to the spacecraft. We had some control over data packetization frequency and found that choosing 0.5 Hz simplified the spike removal process. When the interferograms are transformed into spectra, 8 Hz produces spikes at multiples of 191 cm^{-1} and 0.5 Hz produces spikes at multiples of 12 cm^{-1}. During calibration a deep space reference interferogram is subtracted from each target interferogram and if the spike patterns are matched in both, the spikes cancel. There have been two other types of noise spikes. 1) In May 2007, following a flight software change that regularized some timing effects, a new 1 Hz spike pattern appeared in the interferograms. We eliminated the 1 Hz in July 2008 by reintroducing randomization in the timing. 2) In FP3 there has always been present a spike pattern at 8.33 Hz. Although this pattern would seem to be related to the 8 Hz timing, we never learned its source and have not been able to eliminate it. In general, spike suppression has been much easier in FP1 than in FP3; in FP3 the 8 and 8.33 Hz patterns are mixed and the individual spikes are distorted by the response time of the detectors.

In Fig. 21 FP1 interferograms are presented from three periods during the Saturn mission. Each interferogram is an average of 5000 interferograms recorded on Saturn. Each interferogram is shown expanded so that the 8 Hz and 0.5 Hz patterns can be clearly seen. For each period a raw interferogram and a noise-filtered interferogram are shown. Differences among the three periods are apparent. In the first period, 2004-05, the scan times were multiples of two seconds, so that the positions of the 0.5 Hz spikes repeated from scan to scan. A spike correction algorithm fit a modeled spike comb to the 8 Hz and 0.5 Hz patterns and subtracted them from individual interferograms. After 2006 the 0.5 Hz spikes were further suppressed by choosing scan lengths that shifted the spike positions by 1/16 of their spacing. In averages of multiples of 16 interferograms the 0.5 Hz pattern is converted to an 8 Hz pattern. Large averages of spectra then have a stronger spike at 191 cm^{-1} and its harmonics but suppressed spikes at harmonics of 12 cm^{-1}. In July 2010 we introduced a new modification to the data sampling process that randomizes some of the 8 Hz and thereby reduces the spikes in single spectra. We also began offsetting the 0.5 Hz and remaining 8 Hz patterns by 5 msec in successive interferograms, so that the spikes are eliminated in large averages spectra. In ground calibration we continue to subtract synthetic spike "combs" of 8 Hz and 0.5 Hz patterns from each interferogram to minimize residual spikes [34, 35]. As can be seen in Fig. 21 these measures have been highly successful in cleaning up interferograms. A second type of noise interference has the form of an almost pure sinewave that drifts in frequency and phase in the interferograms. The sinewave frequency is strongly correlated with the temperature of the electronics assembly. The cause is suspected to be temperature drifts of DC-DC power converter frequency, but this has not been confirmed. The sinewave in an interferogram is transformed into a single spike in the corresponding spectrum. As the electronics temperature varied from 22 °C to 17 °C between Jupiter and Saturn the sinewave moved from around 20 cm^{-1} in the FP1 spectra to near 150 cm^{-1} (a weak harmonic has also been found in FP3). Even though the spike is narrow in a single spectrum, it drifts over many scans and broadens in large averages of spectra. Fortunately, its changing location allows selection of spectra where a given region is clear of the sinewave spike. Also, when large averages of spectra are used the drifting phase tends to reduce the sinewave spike. We have developed a process in our noise filter that suppresses the sinewave by fitting and subtracting a synthetic sinewave to each FP1 interferogram [34](Carlson *et al.* 2009). This generally

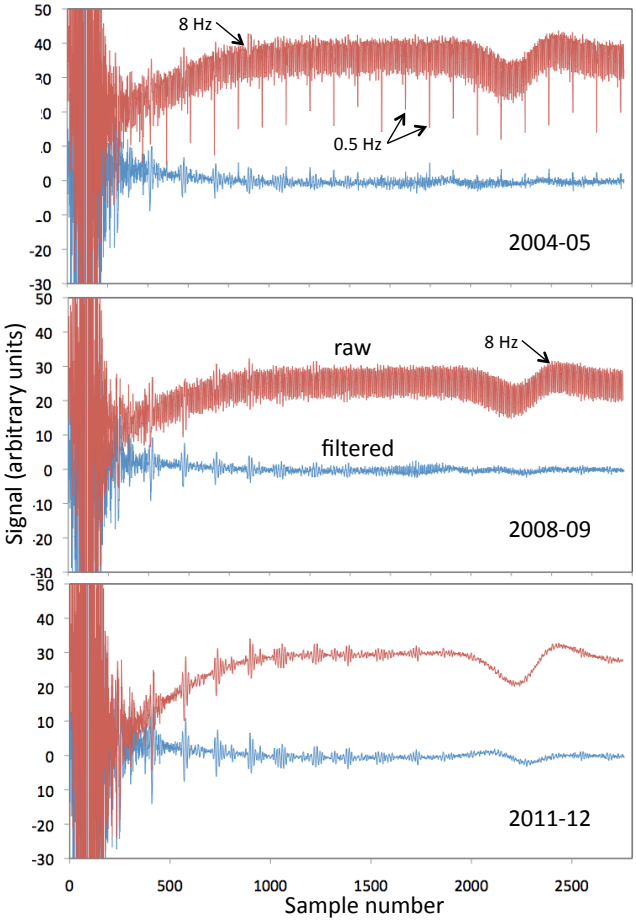

Fig. 21. Averages of raw and filtered interferograms from FP1. Each interferogram is an average of 5000 scans on Saturn. In 2004-05 both 8 Hz and 0.5 Hz spikes were removed by subtracting synthetic combs. A change was made in 2006 to average out the 0.5 Hz spikes, leaving only the 8 Hz spikes in the 2008-09 raw data. In 2010 a further change was made that randomizes and shifts the spike patterns, suppressing them in individual transformed spectra and eliminating them from averages. The filter also removes a baseline from each interferogram by subtracting a synthetic shape that includes the artifact near sample 2200. Burst patterns are due to emission lines in Saturn's spectrum.

reduces the amplitude of the sinewave spike to below the noise level. Noise spikes and sinewave interference are discussed more extensively by Chan *et al.* [36].

D. Reaction wheel interference.

After release of the Huygens Probe in December 2004 we realized that during some periods the recorded interferograms had more samples than normal. Control of the scan mechanism was often lost during these interferograms, making the data useless. The problem was found to be most common during data downlinks to Earth, when the spacecraft was rolling. The cause was tracked to interference from the spacecraft reaction wheel assemblies (RWA's). The reaction wheel rates vary considerably during rolling, over the range 0 to ±1600 rpm [37, 38]. RWA1, 2 and 3 were used at beginning of mission, but because of excess drag RWA3 was swapped with RWA4 in July 2003 and has been used only occasionally since then during checkouts. Fig. 22 shows the disturbance due to each of the three reaction wheels in each year of the Saturn tour. Disturbed scans were identified by extra samples in low resolution (15 cm^{-1}) interferograms beyond the nominal, undisturbed scan length (we used low resolution interferograms because that dataset contained the most scans). Wheel noise causes spurious zero crossings in the reference interferometer, which triggers extra sampling. Besides longer scans, the symptoms included loss of scan mechanism control, premature scan flyback and irregular spacings of the 0.5 Hz noise spikes. Comparing the number of bad interferograms with the wheel rates we found that the disturbances occurred when the wheel rates were above 1300 rpm. Each reaction wheel produces a different pattern of disturbance, but the greatest disturbances in all wheels tended to be between 1300 and 1460 rpm. Of the three wheels, the one that had the greatest detrimental effect was RWA 2 [38].

All indications were that the reaction wheels were causing vibrations in the scan mechanism. The CIRS leaf spring assemblies on the scan mechanism were known to resonate above 20 Hz, close to the 1300 rpm frequency. Although we were able to find some disturbances before 2005, the vibrations became stronger after the release of the probe. (While we were diagnosing the interference from the reaction wheels, a failure occurred in the turntable of LEMMS, the Low Energy Magnetospheric Measurements System. Operation of the turntable produced additional vibration in the scans. The LEMMS turntable failed on February 1, 2005 and was turned off three weeks later.) As fuel has been consumed during the mission the resonant frequencies have increased by an additional amount, particularly in RWA 4 by about 10 Hz between 2005 and 2016. Additional changes in 2004 from Saturn orbit insertion are not shown in the figure.

We address the problem of interference from the reaction wheels by working with the Cassini project to limit wheel rates during CIRS observations. Careful management of the rates has proven successful in minimizing the loss of scientific data. A reaction wheel bias optimization tool was developed at Jet Propulsion Laboratory to provide predictions of the reaction wheel rates, originally to help avoid high-wear rotation speeds. This tool has proven to be crucial in planning CIRS operations for keeping the rates below 1300 rpm. There is still disturbance during rolling downlinks when we collect some of our deep space reference data, but when feasible we have added other non-rolling periods to permit the recording of deep space data.

E. Thermal environment.

Our main purpose for maintaining thermal stability in the instrument is to minimize loss of data. Fluctuations in temperature over the duration of an observation cause calibration errors [39]. We try to avoid pointing the 170 K or 80 K radiator surfaces toward the sun to prevent excessive warming. Even exposing the radiators to a relatively warm planet can drive the instrument out of thermal control, a

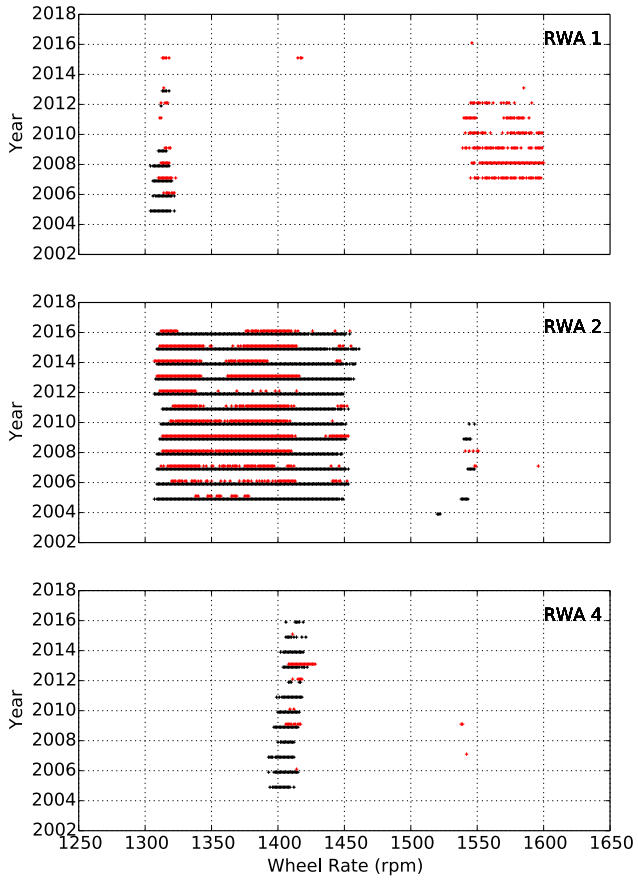

Fig. 22. Disturbance of interferograms as a function of wheel spin rpm for each of the three spacecraft reaction wheels (RWA's). The ordinate is the year and the abscissa is the wheel rate. Positive (red) and negative (black) spin directions are shown overlapped. Most severe disturbances occurred in the 1300-1460 rpm range, predominantly from RWA 2. These data were derived from low resolution (15 cm^{-1}) interferograms.

concern during Saturn orbit insertion and the end-of-mission close-in orbits. This is a particular concern for the 80 K cooler where temperature rises can be fast and recovery times long. The goal is to maintain the CIRS mid-infrared focal plane at as low a temperature as possible to ensure optimum detector sensitivity. We typically operate at 76.3 K, but in cases of extra thermal loading higher temperature setpoints are

available (see next section). A model was developed early in the mission to be used with uplink sequence development tools that predicts the temperature excursions in CIRS during planned spacecraft maneuvers. Based on the model, the focal plane setpoint is adjusted and heaters are commanded in anticipation of temperature swings. Predictions have generally been within 1 K of actual temperatures during observations and have been sufficient to avoid thermal problems. The model has been used successfully during the Saturn tour and improvements continue to be made, the last being implemented in 2014.

9. IN-FLIGHT PERFORMANCE

During flight CIRS has achieved and exceeded the science goals of the investigation. There had been concern during ground testing that the radiance sensitivity was lower than required, and substantial effort was devoted to characterizing the noise and throughput of both the engineering and flight units. To our relief, in flight the sensitivity across the spectrum improved by more than a factor of two over what had been seen during ground testing. This was primarily because the acoustic noise in the thermal-vacuum chamber environment had prevented us from measuring the true noise floor. Fig. 4 shows examples of interferograms from all three focal planes recorded at Saturn. Responses in the mid-infrared depend on the focal plane temperature. Detector response is determined as part of the CIRS calibration process using observations of deep space and shutter. Under minimum heat loading the mid-infrared detector temperatures can be as low as 75.6 K. We can usually maintain the detector temperature at 76.3±0.1 K, but when heat from the sun or Saturn drives the focal plane to a higher temperature we can control at temperatures up to 87 K by selecting one of a number of discrete setpoints. Fig. 23 shows FP3 responses for a single detector at several temperatures in 2002. The response in FP3 decreases with increased temperature over the entire bandwidth from 580 to 1100 cm^{-1}. At 700 cm^{-1} the response decreases by about 30% between 75.6 and 83.6 K. Fig. 23 also shows the same comparison for FP4. In FP4 the responses do not change except at the lowest wavenumbers. At 1100 cm^{-1} the response decreases by 25% between 75.6 and 83.6 K. Sensitivity is characterized by the noise-equivalent spectral radiance (NESR), which gives the source radiance equal to the one-sigma noise level as a function of wavenumber [2, 10]. The temperature dependence of FP3 NESRs in Fig. 23 is dominated by the decrease in response with higher temperature. On the other hand, the FP4 NESRs are dominated by the increase in noise (the response is unchanged with temperature). Thus, although for different reasons, both mid- infrared focal planes degrade in signal-to-noise when the temperature is raised. When FP3 was raised above 87 K it gradually degraded in sensitivity, but when FP4 was raised above 87 K it abruptly stopped working. Both focal planes resumed normal operation when the temperature was decreased.

The long duration of the Cassini mission provides a unique opportunity to investigate the stability of CIRS' sensitivity over time. Comparing 2002 with 2015 in Fig. 24 at a particular focal plane temperature shows that the responses of FP3 and FP4 did not change measurably during the thirteen year period [27, 39]. We estimate that changes were not more than 1% over this time. Noise levels in the 2002 and 2015 spectra are comparable because the numbers of deep space and shutter scans used in each were similar. Our overall impression is that no change in any of the detectors or signal chains has been seen since before launch. For these long-term comparisons the internal temperature, which is used as the absolute reference, must be constant throughout the period. In CIRS the 170 K and 80 K portions of the instrument have been controlled to within 0.1 K during observations. Our measurements assume that the temperature sensors in CIRS have not drifted and that emissivities of the internal surfaces have not changed. We believe that the sensors have been stable because we have seen no long-term change greater than 0.03 K in comparing readings of the control and monitor sensors. Changes in surface emissivity should have little effect because the internal structures that are viewed are

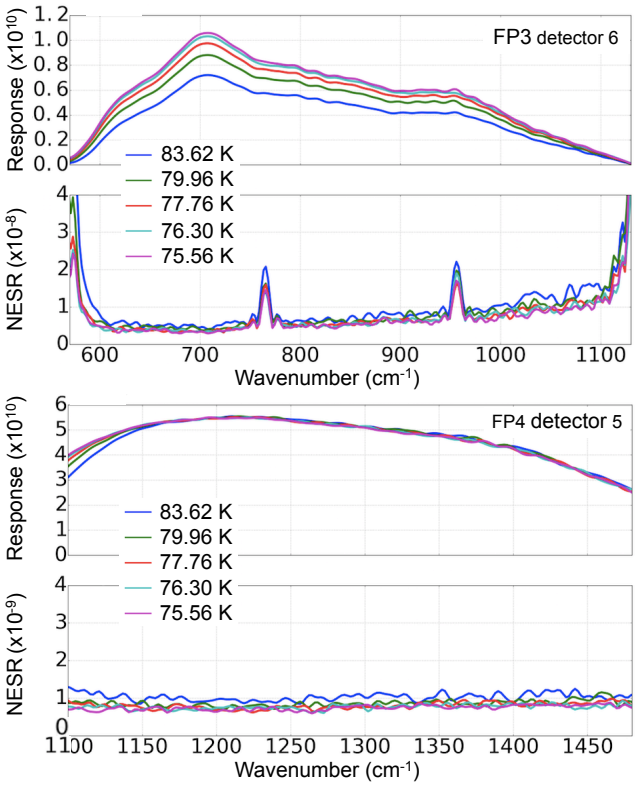

Fig. 23. Detector responses (in signal counts per $W/cm^2/str/cm^{-1}$) and noise-equivalent spectral radiances (NESRs in $W/cm^2/str/cm^{-1}$) for FP3 detector 6 and FP4 detector 5. Responses are at five focal plane temperatures between 75.6 and 83.6 K derived from data recorded in September 2002. Recorded spectral resolution was 3 cm^{-1} and the responses were smoothed to 15 cm^{-1}. For the FP3 responses 99 deep space and 9 closed-shutter scans were used, while for FP4 the numbers were 100 deep space and 10 closed-shutter scans. NESRs are calculated from the standard deviation of the responses. The noise spikes in the FP3 NESRs in 2002 were from harmonics of 8 Hz interference. These were suppressed after 2010 by a change in flight software. The NESR worsens markedly when the detector is operated above 80 K.

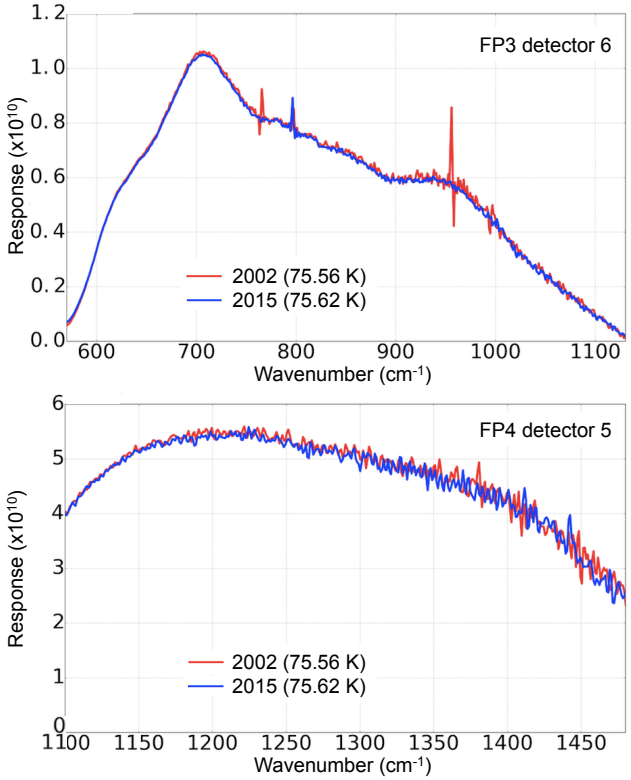

Fig. 24. Comparison of the responses (in signal counts per W/cm^2/str/cm^{-1}) between 2002 and 2015 for FP3 detector 6 and FP4 detector 5. Spectral resolution was 3 cm^{-1} The data were selected to correspond closely to the same focal plane temperature, 75.6 K. The FP3 and FP4 responses in 2002 are the same as in Fig. 23. In 2015 for FP3, 101 deep space and 30 closed-shutter were used, while for FP4 the numbers used were 54 deep space and 16 closed-shutter. The response did not change measureably over the period of the Saturn tour.

surrounded by surfaces at the same temperature and so behave as nearly ideal blackbodies.

CIRS uses DC/DC power converters that might be expected to fail after long exposure to neutrons. Testing of converters containing optical couplers [40] showed that the neutron flux from the radioisotope thermoelectric generators (RTGs) on Cassini would eventually, after about 15 years, cause loss of power in the instrument. The RTGs were installed on the spacecraft adjacent to CIRS in 1996, from which failure would be expected to occur around 2012. Fortunately, as of 2017, we had not seen any significant degradation in performance. Among the various CIRS voltages the largest change was 10 millivolts in a 15 volt supply. The reason for the longer-than-predicted life of the power converters is not known, but could be due to extra shielding of the CIRS electronics by the optics assembly.

10. EXAMPLES OF SPECTRA

The quality of CIRS data is best demonstrated with examples. Figures 25-27 show composite spectra from Jupiter, Saturn, and Titan recorded at 0.5 cm^{-1} resolution. Each of these spectra is a combination of all three focal planes, covering 10-1500 cm^{-1}. The signal is expressed as brightness temperature, which is more convenient than radiance for displaying intensity over the full range of CIRS. Brightness temperature indicates the temperature of the atmosphere or surface where the thermal emission originates. In the Titan spectrum, for example (Fig. 27), emission at 530 cm^{-1} comes from the ~94 K surface, while at 30 cm^{-1} we see the ~65 K tropopause and at 1100 cm^{-1} we are detecting the ~110 K stratosphere. Differences in atmospheric composition and temperature are clearly demonstrated by comparing these spectra. Jupiter and Saturn have hydrogen (H_2) atmospheres, while Titan has a nitrogen (N_2) atmosphere with very little hydrogen. All three atmospheres contain the basic hydrocarbons methane (CH_4), acetylene (C_2H_2), ethane (C_2H_6), and ethylene (C_2H_4). However, ammonia (NH_3) is more visible in Jupiter than in Saturn, and Saturn has phosphine (PH_3) which does not appear prominently in Jupiter. Neither ammonia nor phosphine are found in the Titan spectrum. Nitriles are abundant in Titan's atmosphere, as is apparent from the strong bands of hydrogen cyanide (HCN), cyanoacetylene (HC_3N) and cyanogen (C_2N_2). Table 2 lists the molecular bands and other emission features that CIRS has observed in Jupiter, Saturn and Titan.

CIRS observations of objects without atmospheres, such as Saturn's other moons, its rings and the moons of Jupiter, typically measure thermal emission from surfaces. These measurements are normally performed at reduced spectral resolution, 1, 3 or 15 cm^{-1}, because narrow gaseous features are not expected. As an example, Spilker *et al.* [41] reported radial mapping by CIRS of thermal emission from the rings as a function of solar phase angle, revealing that the ring particles undergo slow rotation. Similarly, Howett *et al.* [42] measured thermal inertia and bolometric Bond albedos on the moons Mimas, Enceladus, Tethys, Dione, Rhea and Iapetus. Perhaps the most important and unexpected result from an icy surface was the CIRS discovery, reported by Howett *et al.* [43], of relatively hot locations along the fissures, or "Tiger Stripes," at Enceladus' South Pole that are associated with plumes. We have developed a specialized method to trace these heat signatures. The technique has

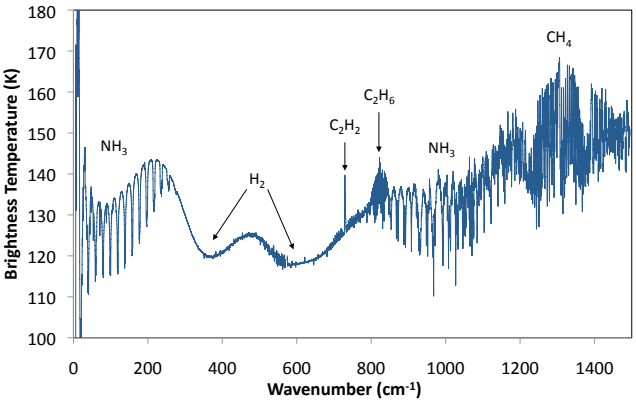

Fig. 25. Brightness temperature spectrum of Jupiter combining data from all three focal planes (FP1, FP3 and FP4). Spectral resolution is 0.5 cm^{-1}. For this dataset emission angles were kept below 50°. Prominent atmospheric features are identified by their molecular species.

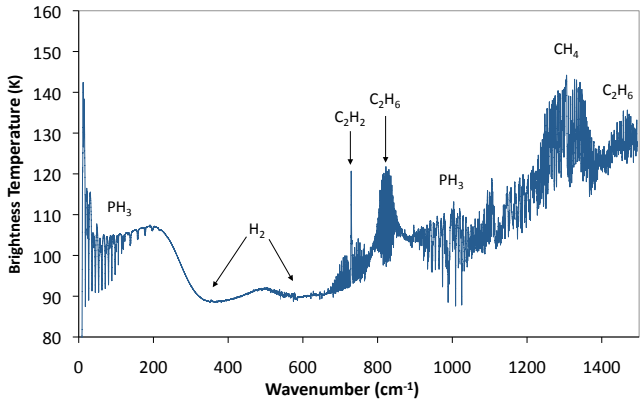

Fig. 26. Brightness temperature spectrum of Saturn combining data from all three focal planes (FP1, FP3 and FP4). Spectral resolution is 0.5 cm^{-1}. For this dataset emission angles were kept below 50°. Prominent atmospheric features are identified by their molecular species.

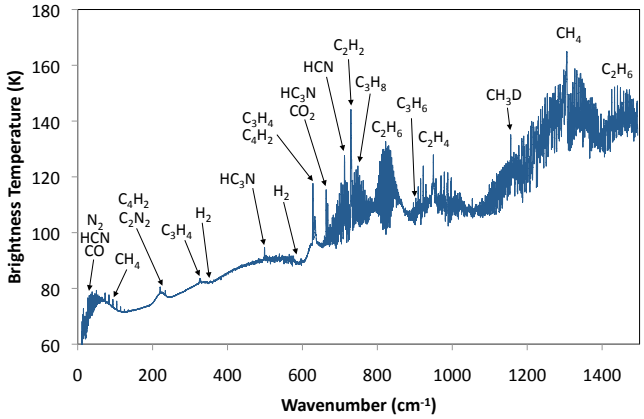

Fig. 27. Brightness temperature spectrum of Titan combining data from all three focal planes (FP1, FP3 and FP4). Spectral resolution is 0.5 cm^{-1}. For this dataset latitudes were restricted to 60-90 North latitude and emission angles were kept below 50°. Prominent atmospheric features are identified by their molecular species.

been described by Spencer *et al.* [44] and Gorius *et al.* [45]. During low-altitude Cassini flybys of the warm fissures, as the path of CIRS' field of view crosses the features, the thermal emission rises and falls rapidly. The brief increases of emission cause transient distortions in the interferogram. In these observations CIRS is acting as a differential radiometer in that it is measuring the change in emission from each thermal feature. Fig. 28 shows a sweep of FP1 across the active South Pole region during the close flyover of Enceladus on April 14, 2012. Cassini came as close to the surface as 75 km at a speed of 7.5 km/sec. Transient signals can be seen in the interferograms as FP1 crossed onto the dark side of Enceladus, passed over numerous warm features on the moon's surface including Baghdad Sulcus (the strongest transient), and moved off the bright limb of Enceladus. At each surface feature the magnitude of the transient provides a measure of temperature change, while the temporal width indicates spatial extent. CIRS was operating in its normal scanning manner during these observations. We used long scans (corresponding to 0.5 cm^{-1} resolution) because they provided long, uninterrupted time periods between carriage flybacks. Three interferograms compose the sweep in Fig. 28 and two of the ZPD bursts occurred while the field of view was on the moon. FP3 and FP4 produce similar results and because of their much smaller detector sizes they provide better spatial resolution, as small as 25 m.

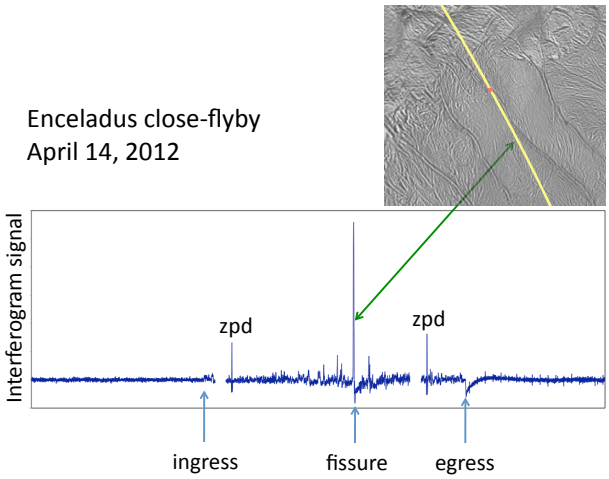

Fig. 28. CIRS used as a differential radiometer during a close pass of Enceladus. FP1 long scans (50 sec) were recorded as Cassini flew over the active southern region on April 14, 2012. Three consecutive interferograms are shown here with two gaps where the carriage returned to start of scan. Deep space reference interferograms have been subtracted from each of these. The ingress and egress limb points are seen where the radiance changed abruptly. As the FP1 field of view passed over narrow, hot features in the vicinity of Baghdad Sulcus the sudden changes in radiance created spikes in the interferogram. Information about the brightnesses and shapes of the emission sources can be derived from these data. (NASA photo.)

11. CONCLUSION

Cassini is ending its mission on September 17, 2017 with a dive into Saturn's atmosphere. During the final "proximal" orbits, beginning in December 2016, the spacecraft will come nearer to Saturn than at any previous time. CIRS will collect data during these close-ups. The rapidly changing thermal environment during these passes presents a challenge to CIRS operations, but we anticipate exciting and unique science results. During the final phase of the mission CIRS plans to operate various backup components that were never or rarely activated during the mission, including the redundant laser and the parallel detector circuit in FP1. FP3 and FP4 will be subjected to high temperatures. Information from end-of-mission tests will be valuable as verification of operation after 20 years in space. We face the final act with sadness, but also with gratification at the amazing success of CIRS and Cassini. We anticipate that CIRS data will produce new scientific discoveries for decades to come.

Table 2. Molecules Observed by CIRS

Species	Formula	ν (cm^{-1})	Sources[†] [Ref.]
Hydrogen	H_2	354, 587	JST
	HD	88, 178, 265	JS
Nitrogen	N_2	50-100	T
Carbon Monoxide	CO	20-80	T
Hydrogen Cyanide	HCN	30-80, 712	JT
	$H^{13}CN$	706	T*[46]
	$HC^{15}N$	711	T*[46]
Carbon Dioxide	CO_2	667	JST
	$^{13}CO_2$	649	T*[47]
	$CO^{18}O$	663	T*[47]
Water	H_2O	140-260	ST
Acetylene	C_2H_2	729	JST
	$^{13}CCH_2$	728	JST*[48]
	C_2HD	519, 678	T*[49]
Cyanogen	C_2N_2	234	T
Ammonia	NH_3	20-300, 800-1200	JS
	NH_3	1060 (solid)	J*[50]
Phosphine	PH_3	20-250, 900-1200	S
Methyl Radical	CH_3	606	J*[51]
Methane	CH_4	50-150, 1306	JST
	$^{13}CH_4$	1297	JST*[48]
	CH_3D	1156	JT
	$^{13}CH_3D$	1148	T*[52]
Ethylene	C_2H_4	949	JST
Ethane	C_2H_6	288, 790-850	JST
	$^{13}CCH_6$	800-840	JT*[48]
Propene	C_3H_6	912	T*[53]
Diacetylene	C_4H_2	628	JST
	$^{13}CC_3H_2$	622, 627	T*[54]
	$C^{13}CC_2H_2$	628	T*[54]
Dicyanoacetylene	C_4N_2	477 (solid)	T
Methylacetylene	C_3H_4	325, 628-637	JST
Cyanoacetylene	HC_3N	499, 663	T
	HC_3N	506 (solid)	T
	$H^{13}C\ C_2N$	659	T*[55]
	$HC^{13}CCN$	663	T*[55]
	$HC_2{}^{13}CN$	663	T*[55]
Propane	C_3H_8	749	ST
Benzene	C_6H_6	674	JST
	C_6H_6	680 (solid)	T*[56]

[†]J - Jupiter S - Saturn T – Titan
*Measured by CIRS for the first time.

Funding. National Aeronautics and Space Administration (NASA), Cassini Mission, CIRS investigation; CNES (Centre National d'Etudes Spatiales; CNRS (Centre National de la Recherche Scientifique, France); SERC (Science and Engineering Research Council, United Kingdom).

Acknowledgement. The authors wish to thank the many people who contributed to the development and operation of CIRS. We acknowledge the support of Goddard Space Flight Center, NASA and the Cassini Project at Jet Propulsion Laboratory.

References

1. V. G. Kunde, P. Ade, R. Barney, D. Bergman, J. F. Bonnal, R. Borelli, D. Boyd, J. Brasunas, G. Brown, S. Calcutt, R. Courtin, J. Cretolle, J. Crooke, M. Davis, S. Edberg, R. Fettig, M. Flasar, D. Glenar, S. Graham, J. Hagopian, C. Hakun, P. Hayes, L. Herath, L. Horn, D. Jennings, G. Karpati, C. Kellebenz, B. Lakew, J. Lindsey, J. Lohr, J. Lyons, R. Martineau, A. Martino, M. Matsumura, J. McCloskey, T. Melak, G. Michel, A. Morell, C. Mosier, L. Pack, M. Plants, D. Robinson, L. Rodriguez, P. Romani, W. Schaefer, S. Schmidt, C. Trujillo, T. Vellacott, K. Wagner, and D. Yun, "Cassini infrared Fourier spectroscopic investigation," Proc. SPIE **2803**, 162–177 (1996).
2. F. M. Flasar, V. G. Kunde, M. M. Abbas, R. K. Achterberg, P. Ade, A. Barucci, B. Bézard, G. L. Bjoraker, J. C. Brasunas, S. Calcutt, R. Carlson, C. J. Cesarsky, B. J. Conrath, A. Coradini, R. Courtin, A. Coustenis, S. Edberg, S. Edgington, C. Ferrari, T. Fouchet, D. Gautier, P. J. Gierasch, K. Grossman, P. Irwin, D. E. Jennings, E. Lellouch, A. A. Mamoutkine, A. Marten, J. P. Meyer, C. A. Nixon, G. S. Orton, T. C. Owen, J. C. Pearl, R. Prange, F. Raulin, P. L. Read, P. N. Romani, R. E. Samuelson, M. E. Segura, M. R. Showalter, A. A. Simon-Miller, M. D. Smith, J. R. Spencer, L. J. Spilker, and F. W. Taylor, "Exploring the Saturn system in the thermal infrared: the composite infrared spectrometer," Space Sci. Rev. **115**, 169–297 (2004).
3. D. E. Jennings, V. G. Kunde, F. M. Flasar and CIRS Team, "The Composite Infrared Spectrometer on Cassini: 15 years in Flight," International Workshop on Instrumentation for Planetary Missions, Greenbelt Maryland, p. 1045, 10-12 October 2012.
4. R. A. Hanel, B. Schlachman, F. D. Clark, C. H. Prokesh, J. B. Taylor, W. M. Wilson, and L. Chaney, "The Nimbus 3 Michelson Interferometer," Applied Optics **9**, 1767-1774 (1970).
5. R. A. Hanel, B. Schlachman, D. Rogers and D. Vanous, "Nimbus 4 Michelson Interferometer," Appl. Opt **10**, 1376-1382 (1971).
6. R. A. Hanel, R. A., B. Schlachman, E. Breihan, R. Bywaters, F. Chapman, M. Rhodes, D. Rodgers, and D. Vanous, "Mariner 9 Michelson Interferometer," Applied Optics **11**, 2626-2634 (1972).
7. R. A. Hanel, R. A., D. Crosby, L. Herath, D. Vanous, D. Collins, H. Creswick, C. Harris, and M. Rhodes, Applied Optics, "Infrared spectrometer for Voyager," Applied Optics **19**, 1391-1400 (1980).
8. D. H. Martin, "Polarizing (Martin-Puplett) interfero-metric spectrometers for the near- and submillimeter spectra," in *Infrared and Millimeter Waves, Systems and Components*, K.J. Button (ed.), Vol. 6, (Academic Press, 1982), Ch. 2.
9. D. H. Martin and E. Puplett, "Polarised interferometric spectrometry for the millimetre and submillimetre spectrum," Infrared Phys. **10**, 105–109 (1969).
10. R. A. Hanel, B. J. Conrath, D. E. Jennings, and R. E. Samuelson, in *Exploration of the Solar System by Infrared Remote Sensing* (Cambridge University Press, 1992, 2003).
11. M. D. Smith, "CIRS Field-of-View Overview," CIRS internal document (2003).
12. P. W. Maymon, M. G. Dittman, B. A. Pasquale, D. E. Jennings, K. I. Mehalick, C J. Trout, "Optical design of the composite infrared spectrometer (CIRS) for the Cassini mission," Proc. SPIE **1945**, pp. 100-111 (1993).
13. R. A. Hanel, B. J. Conrath, D. Gautier, P. Gierasch, S. Kumar, V. G. Kunde, P. Lowman, W. MaGuire, J. C. Pearl, J. Pirraglia, C. Ponnamperuma and R. E. Samuelson, "The Voyager infrared spectroscopy and radiometry investigation," Space Science Reviews **21**, 129-157 (1977).
14. P. Hayes, J. Crooke and B. Perkins, "Cryogenic and ambient testing of the CIRS beryllium telescopes," Proc. SPIE **2227**, 15-25 (1994).
15. P. Losch, J. J. Lyons, and J. Hagopian, "Cryogenic optical performance of the Cassini Composite InfraRed Spectrometer (CIRS) flight telescope," Proc. SPIE **3435**, 19-29 (1998).
16. J.B. Heaney, L. R. Kauder, S. C. Freese and M. A. Quijada, "Preferred mirror coatings for UV, visible, and IR space optical instruments," Proc. SPIE **8510**, F01-F11 (2012).

17. R. A. Keski-Kuha, C. W. Bowers, M. A. Quijada, J. B. Heaney, B. Gallagher, A. McKay and I. Stevenson, "James Webb Space Optical Telescope Element Mirror Coatings," Proc. SPIE **8442**, 84422J (2012).
18. J. A. Crooke, and J. G. Hagopian, "Alignment and cryogenic testing of the Cassini-Composite InfraRed Spectrometer (CIRS) far-infrared (FIR) focal plane," Proc. SPIE **2814**, 105-114 (1996).
19. J. A Crooke and J. G. Hagopian, "Alignment and polarization sensitivity study for the Cassini-Composite InfraRed Spectrometer (CIRS) Far InfraRed (FIR) Interferometer," Proc. SPIE **3435**, 30-41 (1998).
20. R. Fettig, B. Lakew, J. Brasunas, J. A. Crooke, C. Hakun, and J. Orloff, "Thermoelectric infrared detectors with improved mechanical stability for the Composite Infrared Spectrometer (CIRS) far infrared focal plane," Proc. SPIE **3435**, 126-135 (1998).
21. J. G. Hagopian, P. A. Losch and J. A. Crooke, B. Mott, A. J. Martino, "Shear/defocus sensitivity of the mid infrared channel (MIR) of the Composite infrared spectrometer (CIRS) for the Cassini mission to Saturn," Proc. SPIE **3435**, 42-51 (1998).
22. C. A. Nixon, N. A. Teanby, S. B. Calcutt, S. Aslam, D. E. Jennings, V. G. Kunde, F. M. Flasar, P. G. Irwin, F. W. Taylor, D. A. Glenar and M. D. Smith, "Infrared limb sounding of Titan with the Cassini Composite InfraRed Spectrometer: effects of the mid-infrared detector spatial responses," Appl. Opt. **48**, 1912-1925 (2009).
23. R. J. Martineau, Kelley Hu, S. Manthripragada, C. A. Kotecki, S. Babu, F. A. Peters, A S. Burgess, D. B. Mott, D. J. Krebs, S. Graham, A. J. Ewin, A. Miles, V. Bly, T. L. Nguyen, J. McCloskey, P. K. Shu, "HgCdTe Detector Technology and Performance for the Composite Infrared Spectrometer (CIRS)/Cassini Mission," Proc. SPIE **2803**, 178-186 (1996).
24. S. Calcutt, F. Taylor, P. Ade, V. G. Kunde, and D. E. Jennings, "The Composite Infrared Spectrometer," J. of the British Interplanetary Society **45**, 811-816 (1992).
25. A. J. Martino, and D. M. Cornwell, "Reference interferometer using a semiconductor laser/LED reference source in a cryogenic Fourier-transform spectrometer," Proc. SPIE **3435**, 61-71 (1998).
26. R. C. Carlson, D. E. Jennings, J. C. Brasunas, and V. G. Kunde, "Wavelength Calibration of the Cassini Composite Infrared Spectrometer (CIRS) Using Spectrum De-Stretching," in *Fourier Transform Spectroscopy/ Hyperspectral Imaging and Sounding of the Environment*, OSA Technical Digest Series, (Optical Society of America 2005), paper FWD3.
27. J. Brasunas, A. Mamoutkine, and N. Gorius, "Identifying sampling comb changes in Fourier transform spectrometers with significant self-emission and beam splitter absorption," Appl. Opt. **54**, 5461–5468 (2015).
28. A. Tyler, "Shutter Mechanism for Calibration of the Cryogenic Diffused Infrared Background Experiment (DIRBE) Instrument," presented at 20th Aerospace Mechanisms Symposium (NASA-CP-2423-Rev), 97-102 (1986).
29. C. F. Hakun, and K. A. Blumenstock, "A Cryogenic Scan Mechanism for use in Fourier Transform Spectrometers," presented at the 29th Aerospace Mechanisms Symposium, NASA Johnson Space Center, pp. 316-333 (1 May 1995).
30. G. Michel, and R. Courtin, "A Prototype Scan Mechanism for Composite Infrared Spectrometer – CIRS - of the NASA/ESA Cassini Mission," Proceedings of the Sixth European Space Mechanisms & Tribology Symposium, Zurich, 4-6 October 1995 (ESA SP-374, August 1995).
31. J. J. Lyons and P. A. Hayes, "High-optical-quality cryogenic hollow retroreflectors," Proc. SPIE **2540**, 94-100 (1995).
32. H. E. Revercomb, H. Buijs, H. B. Howell, D. D. Laporte, W. L. Smith, and L. A. Sromovsky, "Radiometric calibration of IR Fourier transform spectrometers: solution to a problem with the high-resolution interferometer sounder," Appl. Opt. **27**, 3210–3218 (1988).
33. J. Brasunas, A. Mamoutkine, N. Gorius, "Simple parametric model for intensity calibration of Cassini composite infrared spectrometer data," Appl. Opt. **55**, 4699-4705 (2016).
34. R. C. Carlson, E. A. Guandique, D. E. Jennings, S. H. Pilorz and V. G. Kunde, "Characterization and Suppression of Electrical Interference - Spikes, Periodic Waves, and Ripples - From Cassini Composite Infrared Spectrometer (CIRS) Spectra," in *Advances in Imaging*, Optical Society of America Technical Digest, paper FTuA5 (2009).
35. R. C. Carlson, "Removing Artifacts in the Calibration of Cassini CIRS Spectra of Saturn and Titan," presented at the EPSC-DPS Joint Meeting, Nantes, France (2-7 October 2011).
36. C. Chan, S. A. Albright, N. J. P. Gorius, J. C. Brasunas, D. E. Jennings, F. M. Flasar, R. C. Carlson, E. Guandique and C. A. Nixon, "Electrical Interferences Observed in the Cassini CIRS Spectrometer," Experimental Astronomy **3**, 367–386 (2015).
37. A. Y. Lee, and E. K. Wang, "In-Flight Performance of Cassini Reaction Wheel Bearing Drag in 1997–2013," J. Spacecraft & Rockets **52**, 470-480 (2015).
38. T. S. Brown, "The Cassini Reaction Wheels: Drag and Spin-Rate Trends from an Aging Interplanetary Spacecraft at Saturn," presented at the AIAA Guidance, Navigation, and Control Conference, AIAA SciTech Forum (AIAA 2016-2085), San Diego, California, USA, (4-8 January 2016).
39. J.C. Brasunas and B. Lakew, "Long-term stability of the Cassini Fourier transform spectrometer en route to Saturn," in *Recent Research Developments in Optics*, A. Gayathri, ed. (Research Signpost, 2004), Vol. 4, pp. 95–113.
40. R. Reed, K. LaBel, H. Kim, H. Leidecker and J. Lohr, "Test Report of Proton and Neutron Exposures of Devices that Utilize Optical Components and are Contained in the CIRS Instrument," at https://www.researchgate.net/publication/237349052, (1997).
41. L. J. Spilker, S. H. Pilorz, B. D. Wallis, J. C. Pearl, J. N. Cuzzi, S. M. Brooks, N. Altobelli, S. G. Edgington, M. Showalter, F. M. Flasar, C. Ferrari, C. Leyrat, "Cassini thermal observations of Saturn's main rings: Implications for particle rotation and vertical mixing," Planetary and Space Science **54**, 1167–1176 (2006).
42. C.J.A. Howett, J.R. Spencer, J. Pearl and M. Segura, "Thermal inertia and bolometric Bond albedo values for Mimas, Enceladus, Tethys, Dione, Rhea and Iapetus as derived from Cassini/CIRS measurements," Icarus **206**, 573–593 (2010).
43. C. J. A. Howett, J. R. Spencer, J. Pearl, and M. Segura, "High heat flow from Enceladus' south polar region measured using 10–600 cm^{-1} Cassini/CIRS data," J. Geophys. Res. **116**, E03003, doi:10.1029/2010JE003718 (2011).
44. J. R. Spencer, N. J. P. Gorius, C. J. A. Howett, D. E. Jennings and S. A. Albright, "The Spatial Distribution of Thermal Emission from Baghdad Sulcus, Enceladus, at 100 meter Scales," American Astronomical Society Division for Planetary Sciences, meeting #44, id.104.06 (2012).
45. N. J. Gorius, J. R. Spencer, C. J. Howett, D. E. Jennings, J. C. Brasunas, and S. A. Albright, "Observing the South Pole of Enceladus using Cassini/CIRS as a Radiometer," Optical Society of America Topical Meeting on Fourier Transform Spectroscopy, Lake Arrowhead, CA, 1–4 March (2015), paper FT3-2.

46. S. Vinatier, B. Bézard and C. A. Nixon, "The Titan $^{14}N/^{15}N$ and $^{12}C/^{13}C$ isotopic ratios in HCN from Cassini/CIRS," Icarus **191**, 712–721 (2007).
47. C. A. Nixon, D. E. Jennings, B. Bézard, N. A. Teanby, R. K. Achterberg, A. Coustenis, S. Vinatier, P. G. J. Irwin, P. N. Romani, T. Hewagama, and F. M. Flasar, "Isotopic Ratios in Titan's Atmosphere from Cassini CIRS Limb Sounding: CO_2 at Low and Midlatitudes," Astrophys. J. Lett. **681**, L101-103 (2008).
48. C.A. Nixon, R.K. Achterberg, S. Vinatier, B. Bézard, A. Coustenis, P.G.J. Irwin, N.A. Teanby, R. de Kok, P.N. Romani, D.E. Jennings, G.L. Bjoraker and F.M. Flasar, "The $^{12}C/^{13}C$ isotopic ratio in Titan hydrocarbons from Cassini/CIRS infrared spectra," Icarus **195**, 778–791 (2008).
49. A. Coustenis, D. E. Jennings, A. Jolly, Y. Bénilan, C. A. Nixon, S. Vinatier, D. Gautier, G. L. Bjoraker, P. N. Romani, R. C. Carlson, "Detection of C_2HD and the D/H ratio on Titan," Icarus **197**, 539-548 (2008).
50. M. H. Wong, G. L. Bjoraker, M. D. Smith, F. M. Flasar and C. A. Nixon, "Identification of the 10-µm ammonia ice feature on Jupiter," Planet. & Sp. Sci. **52**, 385–395 (2004).
51. V. G. Kunde, F. M. Flasar, D. E. Jennings, B. Bézard, D. F. Strobel, B. J. Conrath, C. A. Nixon, G. L. Bjoraker, P. N. Romani, R. K. Achterberg, A. A. Simon-Miller, P. Irwin, J. C. Brasunas, J. C. Pearl, M. D. Smith, G. S. Orton, P. J. Gierasch, L. J. Spilker, R. C. Carlson, A. A. Mamoutkine, S. B. Calcutt, P. L. Read, F. W. Taylor, T. Fouchet, P. Parrish, A. Barucci, R. Courtin, A. Coustenis, D. Gautier, E. Lellouch, A. Marten, R. Prangé, Y. Biraud, C. Ferrari, T. C. Owen, M. M. Abbas, R. E. Samuelson, F. Raulin, P. Ade, C. J. Césarsky, K. U. Grossman, and A. Coradini, "Jupiter's Atmospheric Composition from the Cassini Thermal Infrared Spectroscopy Experiment," Science **305**, 1582-1586 (2004).
52. B. Bézard, C. A. Nixon, I. Kleiner, D. E. Jennings, "Detection of $^{13}CH_3D$ on Titan," Icarus **191**, 397–400 (2007).
53. C. A. Nixon, D. E. Jennings, B. Bézard, S. Vinatier, N. A. Teanby, K. Sung, T. M. Ansty, P. G. J. Irwin, N. Gorius, V. Cottini, A. Coustenis, and F. M. Flasar, "Detection of Propene in Titan's Stratosphere," Astrophys. J. Lett. **776**, L14-19 (2013).
54. A. Jolly, A. Fayt, Y. Benilan, D. Jacquemart, C. A. Nixon, and D. E. Jennings, "The ν_8 Bending Mode of Diacetylene: From Laboratory Spectroscopy to the Detection of ^{13}C Isotopologues in Titan's Atmosphere," Astrophys J. **714**, 852-859 (2010).
55. D. E. Jennings, C. A. Nixon, A. Jolly, B. Bézard, A. Coustenis, S. Vinatier, P. G. J. Irwin, N. A. Teanby, P. N. Romani, R. K. Achterberg, and F. M. Flasar, "Isotopic Ratios in Titan's Atmosphere from Cassini/CIRS Limb Sounding: HC_3N in the North," Astrophysical Journal **681**, L109-111 (2008).
56. S. Vinatier, B. Bézard, S. Lebonnois, N. Teanby, R. K. Achterberg, R. de Kok and D. E. Jennings, "Seasonal variations in Titan's middle atmosphere of Titan during the northern spring derived from Cassini/CIRS observations," American Astronomical Society Division for Planetary Sciences, meeting #46, id.211.16 (2014).